JOURNAL OF GEOPHYSICAL RESEARCH, VOL. 100, NO. C8, PAGES 15,977–15,997, AUGUST 15, 1995

Upper ocean modeling in a coastal bay

Jianping Gan and R. Grant Ingram

Department of Atmospheric and Oceanic Sciences, McGill University, Montreal, Canada

Richard J. Greatbatch

Department of Physics, Memorial University of Newfoundland, St. John's, Newfoundland, Canada

Ping Chen

Program in Atmospheric and Oceanic Sciences, Princeton University, Princeton, New Jersey

Abstract. A numerical model of the upper ocean is developed to study the dynamics and thermodynamics of the Baie des Chaleurs (Gulf of St. Lawrence, Canada). The model has primitive equation dynamics with two active layers embedded with a Niiler-Kraus (Niller and Kraus, 1977) type mixed layer model at the top. Proper open boundary conditions and forcing functions are constructed. The model is eddy-permitting, with a horizontal grid spacing of 2x4 km. An Arakawa C grid scheme is used. Forced by observed wind, atmospheric heat fluxes, river runoff, and appropriate remote forcing (in particular, the Gaspé Current, (GC)), the model demonstrates that the mean cyclonic general circulation pattern in the bay is a consequence of the intrusion of the GC. The strength of the circulation depends on the resultant stress of prevailing westerly winds and the opposing GC intrusion. In the mixed layer, atmospheric heat fluxes and horizontal thermal advection play a key role in the thermal balance at the eastern part of the bay. The local mixed layer fluctuations are controlled by wind and GC induced divergence. The entrainment (and its corresponding heat flux) is important at the western part of the bay and changes the mean mixed layer depth on a timescale of more than a week. Varying GC intensifies the flow variations induced by the wind in the bay and improves simulation results as compared with observations.

1. Introduction

The ocean is driven mainly by dynamic and thermodynamic forcing near its surface. In coastal regions, wind stress can generate offshore Ekman transport and local upwelling. These coastal processes are modified by turbulent processes driven by wind and buoyancy forcing. To simulate these processes, appropriate mixed layer (ML) physics must be constructed. Most ML models applied in ocean studies include differential (closure) and bulk models. The former uses the primitive form of momentum, heat, salt and turbulent kinetic energy (TKE) equations [*e.g., Mellor and Yamada,* 1982]. The equations for the bulk model are integrated over the ML and can be easily incorporated into a layer model. Following the pioneering work of *Kraus and Turner* [1967], the bulk ML model has been modified and developed in many studies [*Denman,* 1973; *Niiler and Kraus,* 1977; *Garwood,* 1977]. In an upper ocean model, the ML communicates with the lower layer by the process of entrainment, which in a layer model should be equal to the difference of "apparent motion" and particle motion at their interface [*de Szoeke and Richman,* 1984]. The entrainment rate is determined from the ML model.

Upper ocean modeling and ML physics have been discussed for the open ocean [*e.g. Schopf and Cane,* 1983, *McCreary and Kundu,* 1988; *Cherniawsky et al.,* 1990] and for global simulation [*Yuen et al.,* 1992]. However, there are few studies in the coastal region. Wind induced coastally trapped waves and upwelling can result in strong offshore water transport in the coastal region, which often plays a major role in changing the mixed layer depth (MLD). Horizontal convergence and divergence greatly modify local water mass characteristics not only by vertical advection but also by horizontal advection. These processes, in turn, have an impact on the entrainment process [*Price,* 1981; *McCreary and Kundu,* 1988]. Nonlocal (e.g., inflow, outflow from open ocean) and nearshore forcing (e.g., river runoff) can also change both the circulation pattern and buoyancy field in the coastal region.

In this paper a 2 1/2 layer, upper ocean model, which includes both dynamics and thermodynamics and

Paper number 95JC01276.
0148-0227/95/95JC-01276$05.00

has two active layers, is developed and applied to the Baie des Chaleurs (BdC) (47.5-48.5°N, 65.5-66.5°W), a semienclosed basin opening to the Gulf of St. Lawrence (GSL) (Figure 1).

The objective of this paper is to investigate the circulation and thermal structure of the BdC under the forcing of wind stress, atmospheric buoyancy forcing, river runoff, and nonlocal forcing. After a brief description of observations from the BdC, a numerical model for the coastal upper ocean, its boundary forcing, and boundary conditions are described in section 3. An overview of the response to different forcing is given in section 4. A summary of results and some concluding remarks are given in section 5.

2. Review of Observations

From June to October of both 1990 and 1991 a number of current meters were moored in the BdC at different depths. Conductivity-temperature-depth (CTD) profiles were taken on north-south transects across the bay at a number of sites including at the location of each current meter mooring (Figure 2). Currents were sampled every 20 min by an Aanderaa current meter (RCM7). There was one CTD cruise in October 1990 and six more in 1991, in which 60 CTD stations were sampled over the whole bay during each cruise. Owing to the logistical problems, time series at some stations were truncated [*van der Baaren et al.*, 1992].

Figures 2a,b show the mean circulation in September 1990 and June 1991 from a full month of current observations. In September 1990 the mean along-shore current was directed westward at the north shore and eastward at the south shore, which formed a cyclonic circulation in the central part of the bay (Figure 2a). A similar circulation was also observed in June 1991 (Figure 2b). The cyclonic circulation appears to reach as far as the western inner part of the bay. A similar circulation pattern was also observed by *Tremblay* [1943] and *Legendre and Watt* [1970]. The near-surface currents along the north shore of the bay were stronger than those in the southern area of the bay. Considering the fact that the near-surface current at station O8 was directed north, while at stations O6 and O7, it was directed west and east, respectively, the existence of a cyclonic circulation is indicated. At the entrance of the bay (station O1) in 1991, mainly eastward currents suggest that the GC separated from the north shore before intruding into the bay near O3. It then bifurcated as it reattached to the north shore. At a depth of 50 m the current at O1 was directed southward. An investigation of bottom drift at the entrance of the bay by *Lauzier* [1967] suggested that the bottom current was toward the west along the north coast and toward the east on the south coast. Despite the fact that only a few current meters were deployed during other observation periods, all observations showed similar characteristics.

Previous investigators [*Tremblay*, 1943; *Legendre and Watt*, 1970] have suggested that the cyclonic circulation in BdC resulted from the intrusion of the Gaspé Current (GC), which is mainly generated by the upwelling in the northwest of the GSL [*Bugden*, 1981]. Part of the GC moves along the coast of the Gaspé peninsula and may intrude into BdC [*Trites*, 1972; *El-Sabh*, 1976]. The speed of the GC near the mouth of the St. Lawrence River ranges from 60 cm s^{-1} to 100 cm s^{-1}, with strong vertical shear [*Tang*, 1980; *Benoit and El-Sabh*, 1985; *Mertz and El-Sabh*, 1988].

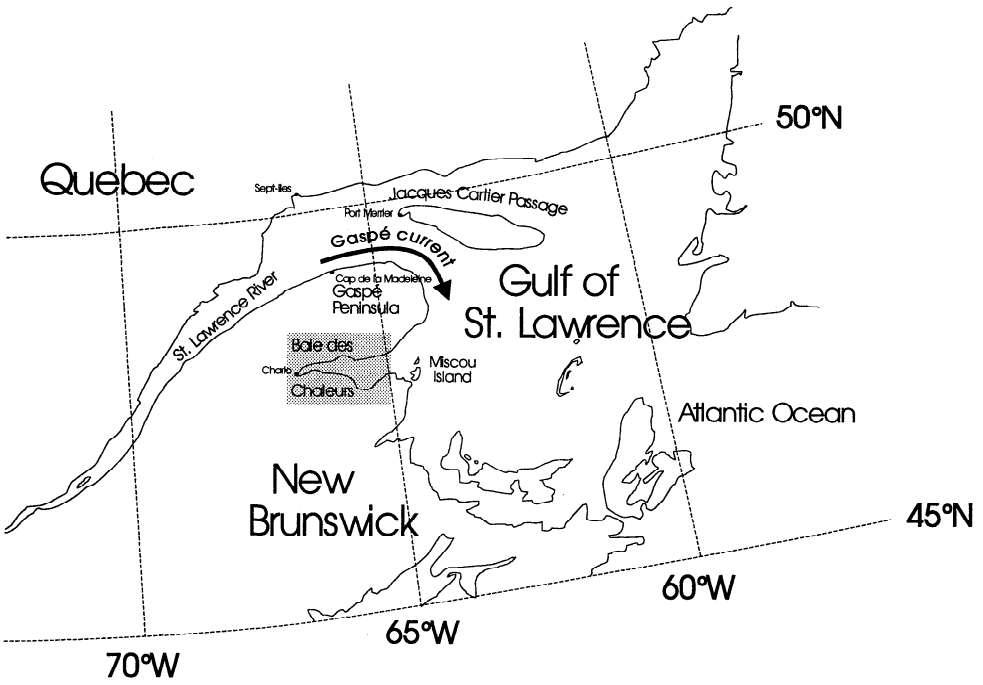

Figure 1. Geographic locations of Gulf of St. Lawrence and Baie des Chaleurs (BdC).

The surface temperature T_1 and salinity S_1 were characterized by a strong gradient in both east-west and north-south directions, as can be seen from the CTD data in 1991 (Figure 3). Lower T_1/higher S_1 water was located at the east entrance of the bay, with temperature/salinity increasing/decreasing toward the inner western part of the bay. The main source of low S_1 water is the runoff from the Matapedia, Restigouche, and Caspedia Rivers in the western part of the bay. Mean runoffs in summer are about 60, 300 and 100 $m^3\ s^{-1}$, respectively, according to historical data [*LeQuere*, 1992]. The temperature/salinity values at the north shore were lower/higher than corresponding values on the south shore. At 25 m depth (not shown) the horizontal gradient of temperature and salinity was weaker. In contrast to the surface layer, warmer and lower-salinity water was located near the bay entrance and at the north shore. The CTD data taken on October 11-12, 1990, (courtesy of M. El-Sabh) also shows similar features in both the surface and deeper layer. They also display distinct cold and salty surface water located east of Miscou Island (Figure 1).

If the water column is divided vertically into two layers with a turbulent ML at the top, higher tempera-

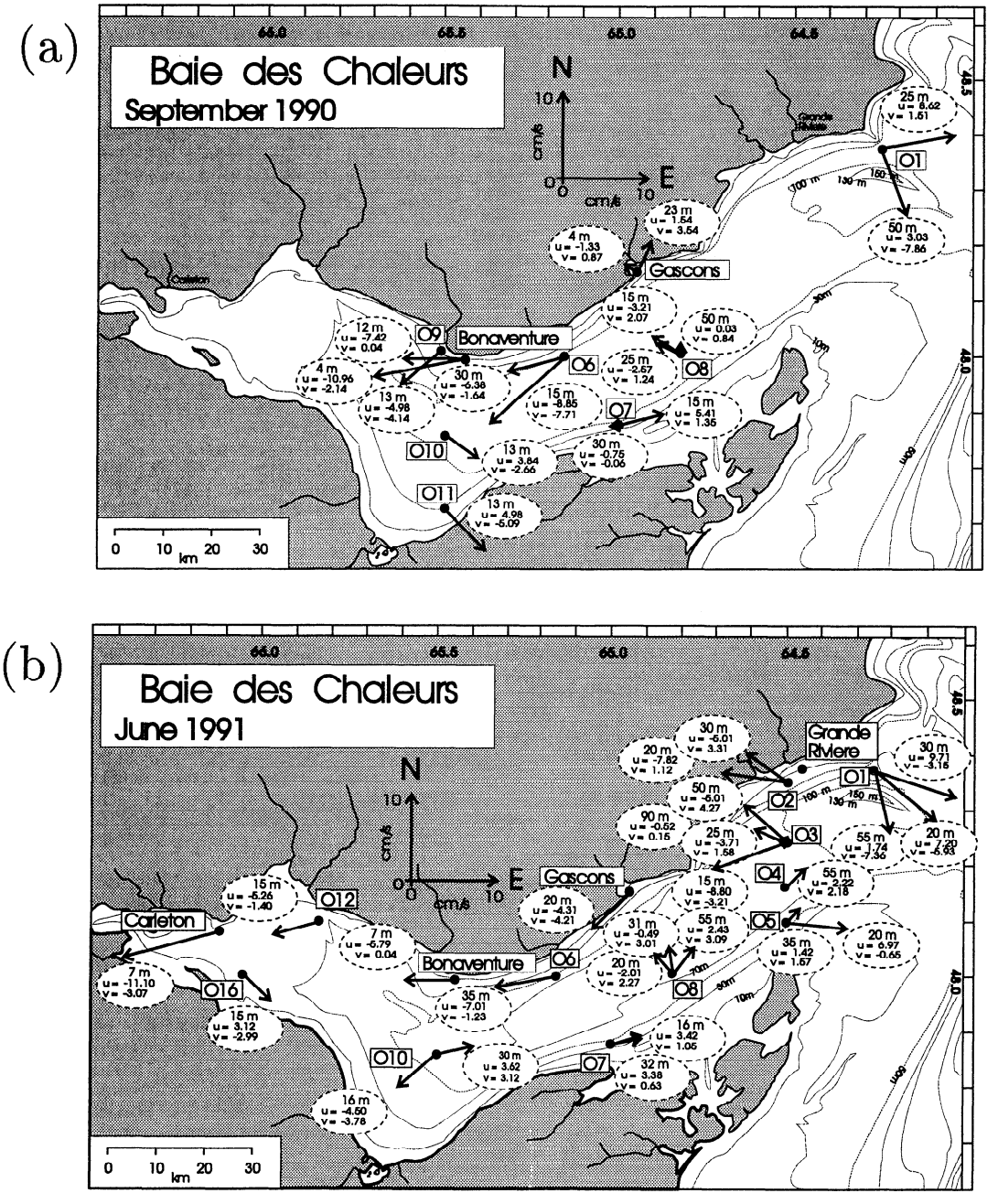

Figure 2. (a) Mean observed circulation in BdC in September 1990 and (b) June 1991. The station numbers are in the rectangular boxes. The u and v in the ovals are the east-west and north-south components of the velocity, respectively. The depth of the current meters are also shown in the ovals.

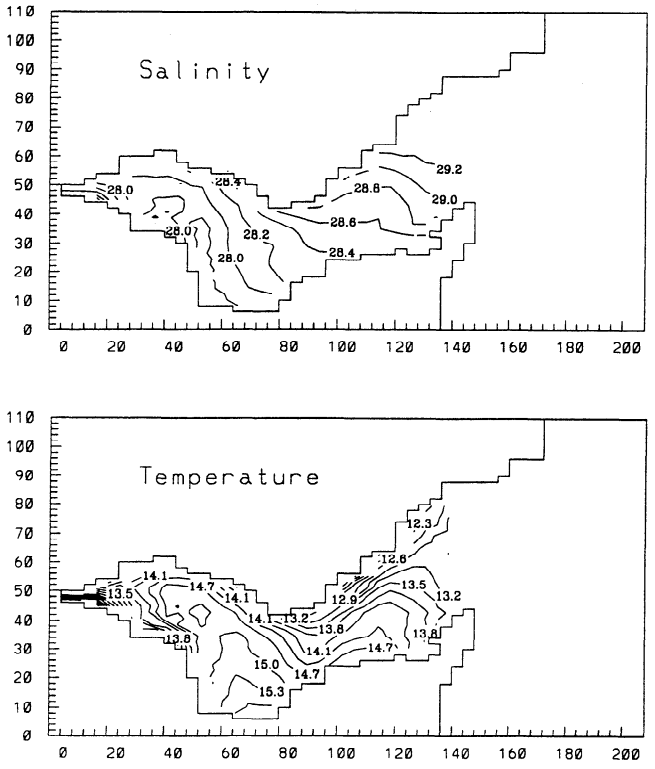

Figure 3. Mean horizontal distribution of temperature (degrees Celsius) and salinity (parts per thousand) in the mixed layer in August and September of 1991.

ture and lower salinity at the lower observed level near the entrance and along the north shore suggest that a deeper ML occurs at these locations. This also matches the cyclonic circulation in terms of dynamical gradient forcing by the tilt of the interface. Therefore the east-west temperature T_1 and salinity S_1 gradient in the ML can be considered as the consequence of the combined effects of cyclonic circulation and the T_1 and S_1 contrast between the eastern entrance (GSL) and western end of the bay.

Comparing time series of vertical σ_t profiles along the northern (station O6) and southern (station O7) shores (Figure 4) with corresponding wind stress (Figure 5), one finds strong upwelling at O6 when the wind stress was dominated by westerlies. It suggests that upwelling was generated, as near surface water was transported offshore by wind-induced Ekman transport. The almost opposite phase of σ_t between station O6 and O7 indicates that corresponding downwelling occurred on the south shore with a smaller amplitude. Periods of stronger westerly winds but weaker upwelling (e.g., on October 3) may result from increased remote current intrusion (to be discussed later).

Figure 6 shows the mean MLD in summer 1991. We define the MLD to be the upper ocean layer whose depth-averaged temperature is ΔT higher than the water temperature just below. Observations showed that vertical temperature profiles have a deep stratified layer below the ML in BdC, with a temperature span of about 6^0C (Figure 7). Since the density profiles in this paper will be approximated as a two-layer system (see model description in section 3), it is convenient to choose ΔT as 3^0C in the present study. As can be seen from Figure 6, a prominent feature of the MLD distribution in BdC was a deep trough near the entrance which gradually shoaled toward the west, consistent with the thermal fields observed at the 25 m.

3. The Ocean Model

3.1. Model Description

The model consists of two active layers and a deep resting lower layer (Figure 8). The model formulation is similar to that in *Schopf and Cane* [1983]; *McCreary and Kundu* [1988]; *Cherniawsky et al.* [1990]; and Yuen et al. [1992]. The equations for momentum, continuity, temperature, and salinity for the upper and lower layers (i=1, 2) are

$$(h_i\mathbf{V_i})_t + \nabla\cdot(h_i\mathbf{V_i}\mathbf{V_i}) + f\mathbf{K}\times h_i\mathbf{V_i} = \delta_{i1}\frac{\tau_0}{\rho_0} - h_i\nabla P_i + (-1)^{i+1}W_e[H(W_e)\mathbf{V_2} + H(-W_e)\mathbf{V_1}] + \delta_{i2}W_r\mathbf{V_r} + K_u\nabla\cdot(h_i\nabla\mathbf{V_i}) \quad (1)$$

$$(h_i)_t + \nabla\cdot(h_i\mathbf{V_i}) = (-1)^{i+1}W_e + \delta_{i2}W_r \quad (2)$$

$$(h_iT_i)_t + \nabla\cdot(h_i\mathbf{V_i}T_i) = \frac{Q_i}{\rho_0 C_p} + (-1)^{i+1}W_e[H(W_e)T_e + H(-W_e)T_1] + \delta_{i2}W_rT_r + K_m\nabla\cdot(h_i\nabla T_i) + C_{Ti} + \delta_{i2}N_T \quad (3)$$

$$(h_iS_i)_t + \nabla\cdot(h_i\mathbf{V_i}S_i) = (-1)^{i+1}W_e[H(W_e)S_e + H(-W_e)S_1] + \delta_{i2}W_rS_r + K_m\nabla\cdot(h_i\nabla S_i) + C_{Si} + \delta_{i2}N_S \quad (4)$$

Where $\mathbf{V}_1$ and $\mathbf{V}_2$ are horizontal velocities at the ML and the second layer, respectively. The unit vector $\mathbf{K}$ is directed upward. H is the Heaviside step function and δ_{ik} is the Kronecker delta function. τ_0 here is wind stress and C_p is specific heat of water (=4025 J kg^{-1} K^{-1}); $\nabla P_1=\nabla(g_1'\ h_1+\ g_2'h_2)$-$h_1\nabla\ (g_1'/2)$ and $\nabla P_2=\nabla(g_2'h_2/2)+g_2'\nabla(h_1+h_2/2)$ are horizontal pressure gradients at the ML and subsurface layer, respectively. The Coriolis parameter f is kept constant in the model due to small β effect. The g_1' and g_2' are defined as $g_1'=g(\rho_3-\rho_1)/\rho_0$; $g_2'=g(\rho_3-\rho_2)/\rho_0$; ρ_3 is the density of the deep ocean or lowest layer, which remains spatially constant. Density is determined from the equation of state $\rho=\rho(S,T,Z)$. Here g is gravity and ρ_0 is a reference density. K_u and K_m are horizontal eddy viscosity and

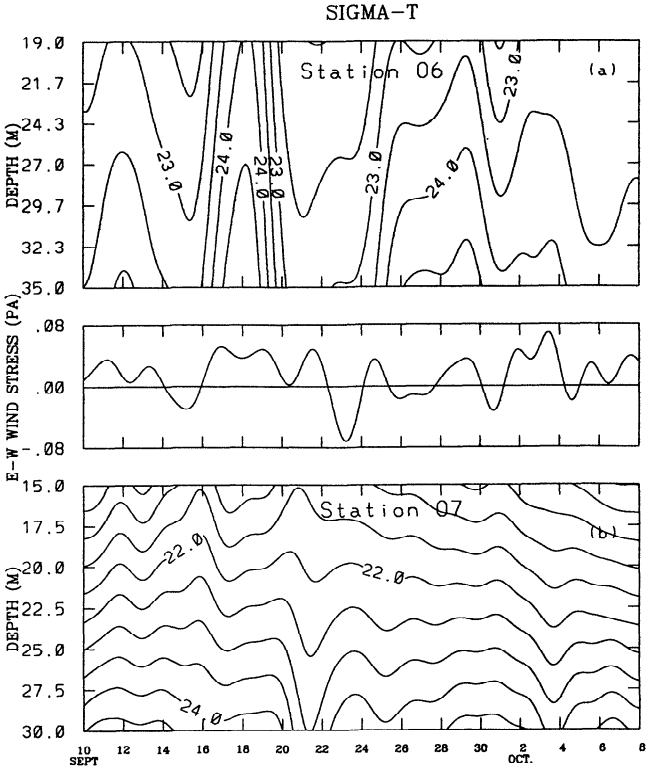

Figure 4. Time series of the east-west wind stress and vertical σ_t profiles at stations O6 and O7.

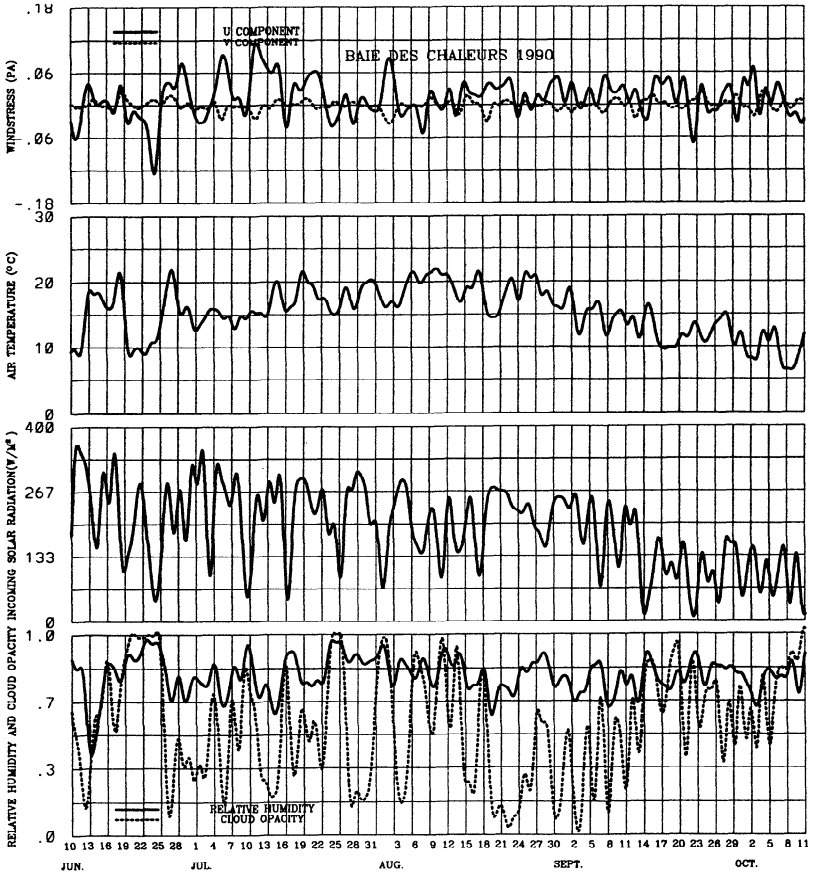

Figure 5. Time series of wind, air temperature, relative humidity, and cloud opacity at station Charlo and incoming solar radiation at Sept-Iles (from Environment Canada). See Figure 1 for the locations.

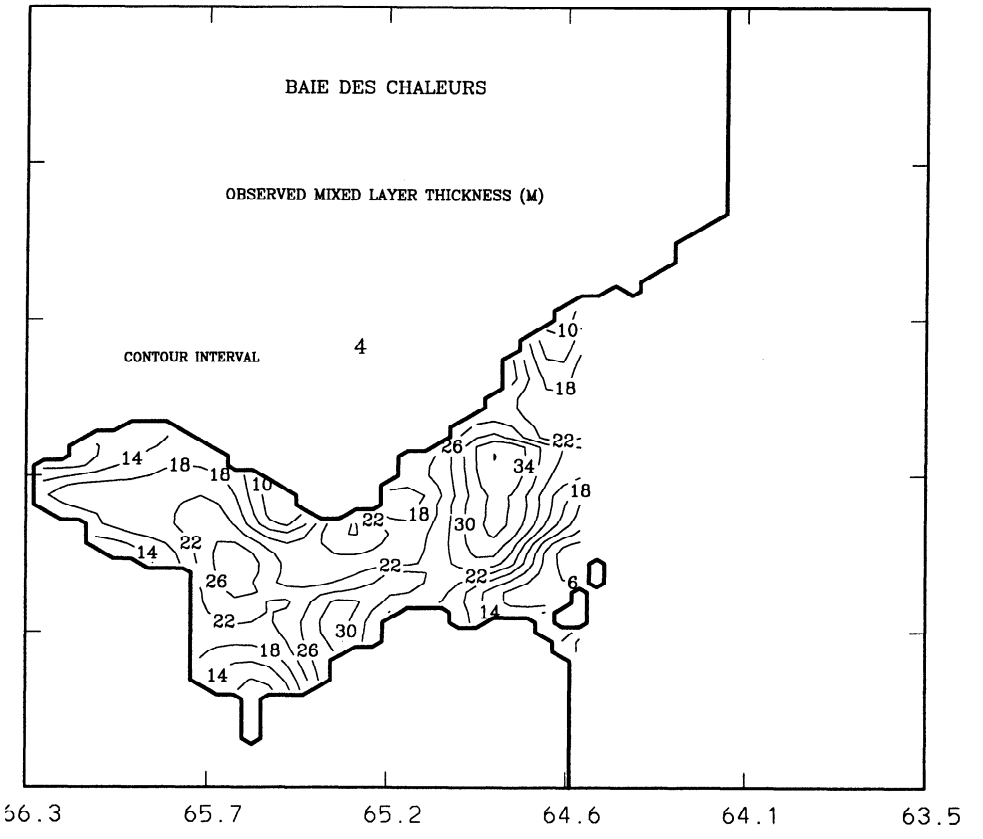

Figure 6. Mean observed mixed layer depth (MLD) calculated from conductivity-temperature-depth (CTD) data from June to October 1991.

diffusivity coefficients (K_u=40 m^2 s^{-1}, K_m=30 m^2 s^{-1}), which have same order of magnitude as estimated from the *Smagorinsky* [1963] formulas. T_e and S_e are the temperature and salinity at the interface between the ML and the layer below. In this study, when $W_e > 0$ (entrainment), T_e and S_e are obtained by assuming linear stratification below the ML [*Schopf and Cane*, 1983]. $T_{1,2}$ and $S_{1,2}$ are defined at the middepth of the layer. Therefore we have $T_e=2T_2-T_3$ and $S_e=2S_2-S_3$. T_3 and S_3 are the temperature and salinity in the deep ocean. When $W_e < 0$ (detrainment), $(T_e,S_e)=(T_1,S_1)$. The surface and interfacial temperature fluxes $Q_{1,2}$ are given by

$$Q_1 = Q_o(1-\mathbf{a}) - L_a - H_a - LE_a - I(0)e^{-h_1/h_s} \quad (5)$$

$$Q_2 = I(0)e^{-h_1/h_s} \quad (6)$$

where Q_o is the measured incoming shortwave radiation at the surface, $\mathbf{a}$ (=0.1) is the albedo of the sea surface, $I(0)$ is the penetrating shortwave radiation where $I(0)=C_r Q_o$ and C_r is the percentage of penetrating shortwave radiation and h_s is the attenuation depth of shortwave radiation. The radiation coefficients are chosen as C_r=0.40 and h_s=15 m, corresponding to water type III following *Paulson and Simpson* [1977]. L_a is longwave radiation, which is calculated following the Berliand formula *Budyko* [1974]. H_a and LE_a are the vertical flux of sensible and latent heat, which are determined from standard bulk formulations [*Gan et al.*, 1995], respectively. L is the latent heat of vaporization (2.5x10^6 J kg^{-1}).

In the model, instantaneous convection between the ML and subsurface layer (C_{T1}, C_{S1}) occurs when $\rho_1 > \rho_2$. A depth-weighted scheme (i.e., $T=[(T_1,S_1)h_1+(T_2,S_2)h_2]/(h_1+h_2)$) is then adopted. When $\rho_2 > \rho_3$, the deep

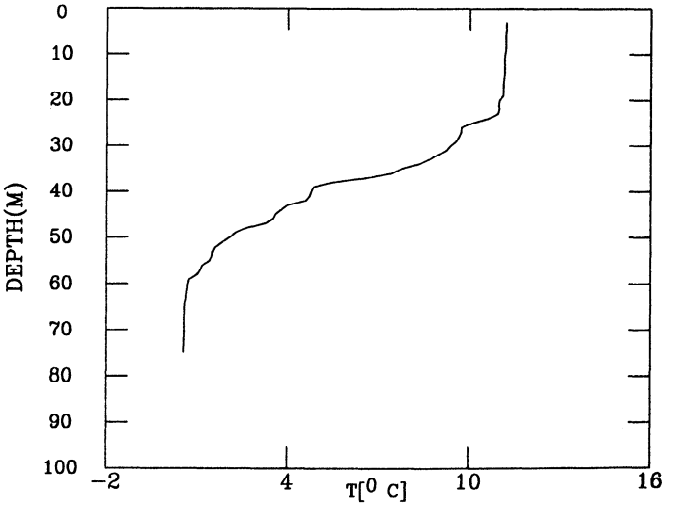

Figure 7. Typical temperature profile in BdC during summer.

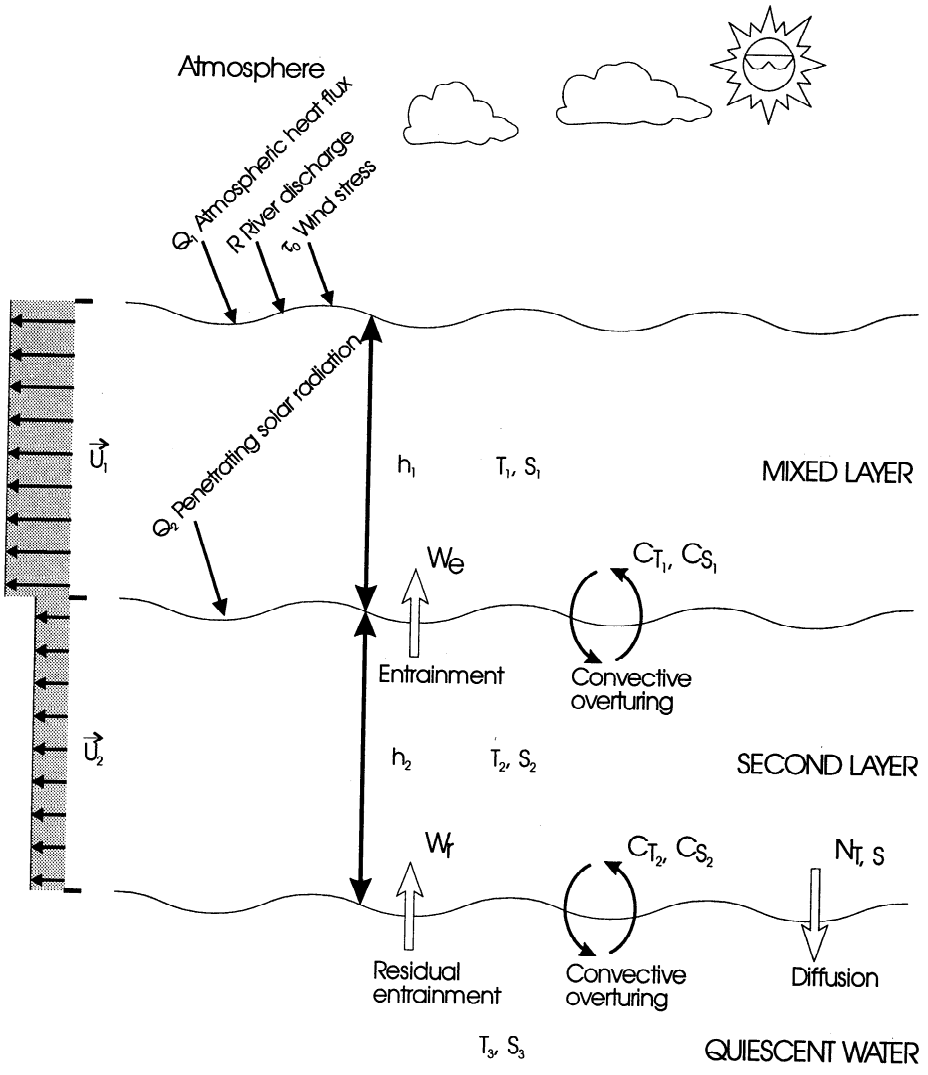

Figure 8. A schematic diagram of the model.

convection scheme between the subsurface layer and the deep ocean occurs. We then set $(T_2,S_2)=(T_3,S_3)$, similar to the method used by *Cherniawsky et al.* [1990] and *Yuen et al.* [1992]. The heat N_T and salt N_S diffusion between the second layer and the deep ocean are defined as $N_T=HN(T_3-T_2)$ and $N_s=HN(S_3-S_2)$, where T_3 and S_3 are the averaged temperature and salinity in the deep ocean. The coupling coefficient is equal to $HN=5\text{x}10^{-7}\text{m s}^{-1}$ which corresponds to a vertical eddy diffusive coefficient of 10^{-5} m^2 s^{-1} for h_2 of 20 m. The vertical diffusion was very close to the value estimated by *Bugden* [1981] in the GSL.

W_e in the model is the entrainment/detrainment rate, which is determined from the *Niiler and Kraus* [1977] type formulation, similar to *Oberhuber* [1992] and can be seen in the work by *Gan et al.* [1995]. The mixing efficiency coefficient associated with wind-driven turbulence is equal to 1.2, and the coefficient associated with frictional energy dissipation of the convective mixing is equal to 0.83 and 1 for positive (ocean gains heat) and negative total buoyancy flux through the surface, respectively. In the model the effect from precipitation minus evaporation on the buoyancy is neglected.

W_r in the equations is defined as the residual entrainment rate at the bottom of the second layer [*Cherniawsky et al.*, 1990; *Yuen et al.*, 1992]. It equals zero except when the second layer is shallower than the prescribed depth H_e (20 m in the model). Nonzero W_r could occur when there is a strong upwelling or the ML is deepening in winter. Also, $\mathbf{V}_r=0$ or $=\mathbf{V}_2$ if $W_r>0$ or <0. For any volume of water entrained from the deeper ocean into the second layer, the same volume of water is evenly deducted everywhere from the second layer in order to keep the mass conserved. In (3) and (4), $(T_r,S_r)=(T_3,S_3)$.

3.2. Numerical Implementation and Model Input

With an internal Rossby radius of about 8 km in BdC, a grid size of $\Delta X\times\Delta Y=2$ km$\times$4 km and an Arakawa C staggered grid were used. A center space difference for the flux form equation was applied in the model, which ensures that certain integral constraints are conserved by the differencing [*Haltiner and Williams,* 1980]. To control small-scale numerical noise and remove time splitting from the leapfrog differencing scheme, a weak

filter [*Asselin,* 1972] was used at each time step. The time step t_e was chosen as 10 min. At the northern, southern, and eastern open boundaries, an Orlanski type radiation scheme was applied to $(h_{1,2})$. It is found that the modified orlanski implicit (MOI) [*Camerlengo and O'Brien,* 1980] radiation condition gives a smoother boundary solution. At the beginning of the model testing, various radiation conditions were also applied to the velocity. However, as the remote forcing was imposed near the coast of the northern boundary (see discussion below), a "noiselike" current seemed to move around the region of the open boundary after a certain time of integration. Therefore we put a zero-gradient condition $\partial \mathbf{V}_i/\partial \mathbf{n}=0$ for along-boundary velocity and calculated the component normal to boundary the same way as in the main program. The operator $\partial/\partial \mathbf{n}$ indicates a partial derivative normal to the boundary. A zero-gradient in layer depth condition $\partial h_{1,2}/\partial \mathbf{n}=0$ was applied on the northern boundary in order to suppress spurious Kelvin wave propagation. The treatment of open boundary conditions here is similar to that suggested by *Greatbatch and Otterson* [1991]. The lateral boundary conditions on the sidewall of the bay are no-slip.

In the case applying the GC at the northern boundary, the southward velocities, which are determined from across-boundary transports, are imposed on the northern boundary at the upper and lower layer, respectively (see section 4.3). The northern open boundary was located at the tip of the Gaspé peninsula (Figure 1). To avoid surfacing of the ML, the minimum h_1 was set to 2 m in the model.

When the flow is into the model domain, the prescribed boundary temperature and salinity are advected into the model domain. The boundary $T_{1,2}$ and $S_{1,2}$ values are from long-term climatological mean data of *Petrie* [1990] and are interpolated linearly for each time step in the study period.

The time frame of this study is from the beginning of August to October 1990, as shown in Figure 5 and can be divided into warm (August to mid-September) and the cooling (mid-September to mid-October) seasons. The wind data were obtained from the Atmospheric Environment Service (AES) of Environment Canada. The prevailing wind in BdC from June to October 1990 was westerly, as shown in Figure 5. In the model, the wind stress was calculated following the formula of *Large and Pond* [1980]. The wind speed in the open bay was estimated from the observed wind speed on land at Charlo (Figure 1) by using the relation suggested by *Hsu* [1986].

The air temperature, incoming solar radiation, relative humidity, and cloud opacity, also from AES, are shown in Figure 5. They were used to calculate the atmospheric heat fluxes in the model.

The physical timescales of interest for our study in BdC are in the subinertial and longer periods. The observed data in this paper have been low-pass filtered to remove energy with periods less than 36 hours.

River runoff at the western part of the bay was specified in the ML at the grid points nearest the river exits. Historical mean runoff data [*LeQuere,* 1992] during the time frame of this study were (approximately) applied for the entire integration period. Rivers with an average runoff of less than 50 $m^3\ s^{-1}$ were neglected. The temperature for river runoff injected into the model domain was approximated as 5^0C lower than T_a.

4. Numerical Results

To test the validity of the model and distinguish between the influence of different forcing regimes, several experiments were conducted. In section 4.1 a constant eastward wind stress was applied to the model to determine the dominant features of the upper ocean response to wind. This test also serves as a verification of the model dynamics. In section 4.2, the observed wind and heat flux were first used to force the model and then the GC was applied in section 4.3. The dynamic and thermodynamic results are compared with the corresponding observations. The thermal balance in the ML, the characteristics of the ML, and variability of the dynamics and thermodynamics are then studied in sections 4.4, 4.5, and 4.6, respectively.

In all experiments, except for the case of constant westerly wind forcing (section 4.1), heat flux will be calculated using observed atmospheric data (Figure 5). The initial mean thermal conditions and layer thickness for the model were estimated from available data near the bay entrance [*Petrie,* 1990] in April. They are summarized in Table 1. After spinning up the model with the observed meteorological forcing (wind stress and heat fluxes) from April to July (Figure 5) which allows the transients (from initial conditions) to dissipate, the results from August to early October were obtained. The latter period contained the longest current meter records for comparison to the model.

4.1. Forcing With Constant Westerly Winds

The model was forced with 0.03 Pa westerly wind stress. The atmospheric heat fluxes in this case were calculated using a constant air temperature of T_a=12°C, incoming solar radiation of S=100 W m^{-2}, relative humidity of 75 % and a cloud cover of 0.5. The initial conditions were the same as Table 1 except T_1 (=10^0C)

Table 1. Initial Values

Variables	Values	Elements
h_1	15 m	upper layer depth
h_2	20 m	lower layer depth
T_1	3.5^0C	surface temperature
T_2	3^0C	low layer temperature
T_3	2^0C	bottom temperature
S_1	28.5 o/oo	surface salinity
S_2	30.5 o/oo	low layer salinity
S_3	31.5 o/oo	bottom salinity
U_1	0 m s^{-1}	upper layer velocity
U_2	0 m s^{-1}	lower layer velocity

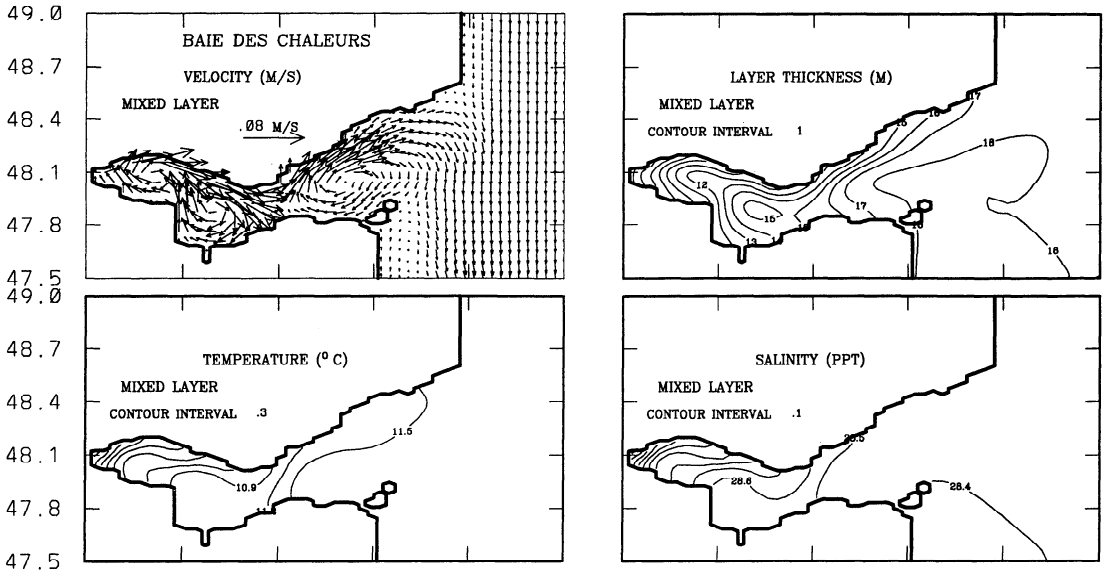

Figure 9. The mean circulation, thickness, temperature, and salinity of the mixed layer (ML) under constant wind stress.

was chosen to be close to the value in June. For simplification, zero normal thermal gradients were applied on the open boundaries in this experiment and the one in section 4.2, when the model was forced by observed winds.

Initially, an eastward current was generated throughout the bay in the ML. After 10 days the eastward current near the south shore gradually decreased and changed to westward, which produced an upper layer anticyclonic circulation pattern in the central region of the bay, with two other weaker eddies located to the west and east of the central one. Figure 9 shows the 61-day mean fields. The Ekman transport at the open GSL generated a southward current. This southward current was negligible at the subsurface layer.

The thickness of the top layer h_1 in the bay gradually adjusted to about 16-20 m after 120 days, and the circulation became very weak. The southward Ekman drift on the north shore produced convergence of the water masses toward the center of the bay and a deeper ML. The shoaling of the ML along the north shore due to upwelling can intensify entrainment by converting mean potential energy to TKE [*Price*, 1981; *McCreary and Kundu*, 1988], (also see section 4.5). This led to decreasing temperature and increasing salinity in the ML (Figure 9). The offshore mass transport which was induced by the westerly wind at the western end of the bay formed a shallower ML there. The corresponding colder and saltier water from the lower layer was entrained into the ML and then advected eastward by the local current. Combined with locally entrained water, it formed a cold and saline water mass in the western part of the bay and along the north shore.

A weak cyclonic circulation occurred in the subsurface layer and the overall temperature and salinity responses were weaker. We also carried out experiments forced by constant easterly, northerly, and southerly winds. The first two cases generated cyclonic circulation patterns, while the third gave anticyclonic motion in the ML.

4.2. Forcing With Observed Winds

When the model was forced with the observed wind and river runoff at the western end of the bay, the 2-month mean circulation (mean field from August 1 to September 30, hereinafter referred to as the 2-month mean) after the spin-up from April was an anticyclonic pattern in the ML, similar to Figure 9 with local eddies. Since the prevailing wind in the BdC was westerly (Figure 5), mean dynamical patterns were quite similar to the results with constant westerly forcing in the last subsection. With the inclusion of river runoff a plume was generated in the western part of the bay. This plume can reach as far as the central part of the bay (Figure 10) depending on westerly wind strength.

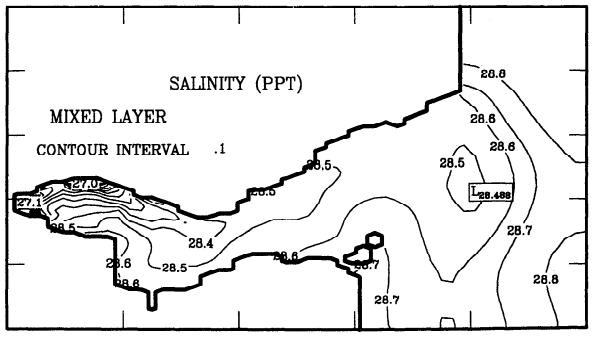

Figure 10. The 2-month mean salinity in the ML for observed atmospheric boundary forcing and river runoff.

4.3. Forcing With Observed Winds and the Gaspé Current

It was shown in section 2.2 that the observed mean circulation in the BdC was cyclonic (Figures 2a and 2b). Given the prevailing westerly winds in BdC (Figure 5), the above model results implied that the circulation in the bay should be anticyclonic instead of cyclonic. As suggested in section 2.2, the cyclonic circulation, in fact, results from the intrusion of the GC.

To account for the influence of the GC in BdC, an inward constant transport of the GC was uniformly applied within 20 km of the coastline [*El-Sabh,* 1976; *Benoit and El-Sabh,* 1985; *Mertz et al.,* 1988] at the northern boundary entrance. The study by J. P. Gan et al., (On the separation/intrusion of unsteady Gaspé current and variability in Baie des Chaleurs, II, Modeling, submitted to *Journal of Geophysical Research,* hereinafter referred to as submitted manuscript, 1995a) shows that effects of changing the GC profile on the circulation in the BdC is not sinificant. Following the characteristics of the GC, transports of 1.3×10^5 m^3 s^{-1} and 1.4×10^4 m^3 s^{-1} along the east coast of the Gaspé peninsula were applied in the ML and subsurface layer, respectively. The GC values in this study are about 45% of the running mean transport from *Bugden* [1981, Figure 2.9] . The remainder can be accounted for by the portion that diverges toward the Laurentian Channel and Magdalen Shallows [*Trites,* 1972; *El-Sabh,* 1976]. Both *Bugden* [1981] and *Mertz et al.,* [1991] found that the lowest mean GC transport occurred in July and rapidly increased toward August. Therefore the Bugden's monthly GC transport values (courtesy of G. L. Bugden) were used in the period of spin-up and linearly

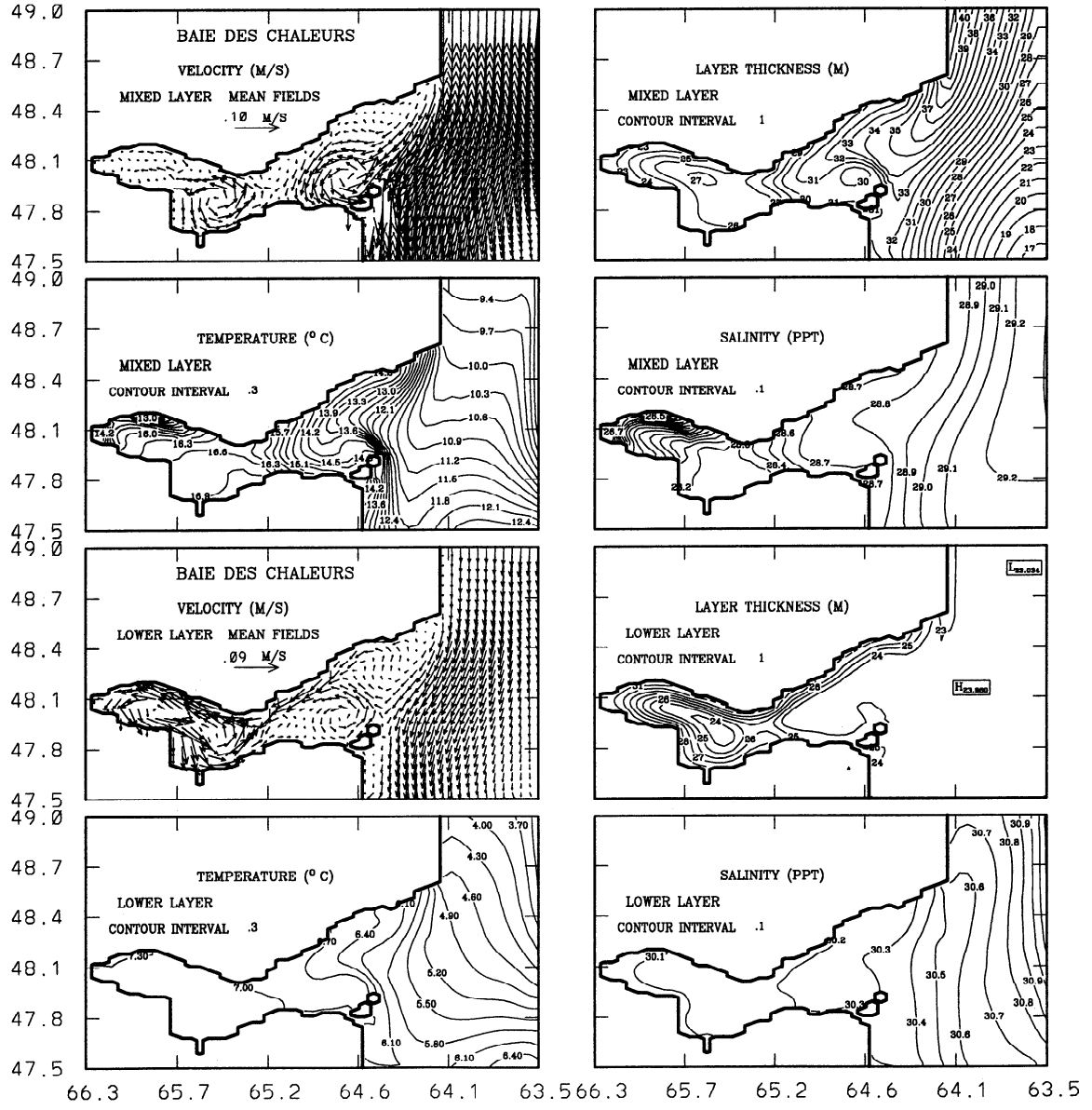

Figure 11. The 2-month mean circulation, temperature, salinity, and thickness of ML for observed atmospheric boundary forcing, Gaspé Current, and river runoff in the mixed layer and subsurface layer. The current speed is truncated at 0.1m s^{-1}.

increased to 1.3×10^5 m^3 s^{-1} in August. The present study considers the results from steady GC forcing while the unsteady GC is discussed by Gan et al. (submitted manuscript, 1995a). The current strength of the GC corresponds to about 20 cm s^{-1} and 3.5 cm s^{-1} for the 30 m MLD and 20 m subsurface layer depth, respectively. These are close to the mean observed summer speeds in the region [*Gregory et al.*, 1989; *Benoit and El-Sabh*, 1985]. The effect of the GC strength will be examined later in text.

By including the GC input at the northern entrance, the 2-month mean field (Figure 11) showed that h_1 sloped down from west to east. Dynamically, the GC intrusion caused a nearshore downwelling and deepened the ML along the coast near the entrance. The deeper ML was later advected into the bay as a result of the dynamical imbalance between the prevailing westerly wind and the GC, as well as by internal Kelvin waves. If the GC was constantly applied, it led to the formation of cyclonic circulation in the bay (Figure 11). In contrast, an eastward component of wind stress tended to reduce this pressure gradient. Clearly, the strength of the circulation in the bay depends on the relative strength of the prevailing wind stress and the intruding GC. The cyclonic circulation implied that the GC intrusion was a dominant factor. The stronger influence of the GC on the north shore and the weaker eastward current on the south shore caused a NW-SE orientation of the MLD contours (Figure 11) near the center of the bay.

It can be seen that the GC left the north shore near the salient edge as it moved southward along Gaspé peninsula. It mainly entered the bay north of Miscou Island. The current reattached on the north shore, bifurcated, and generated cyclonic and weak anticyclonic eddies to the west and north of Miscou Island, respectively. Numerical experiments with a much weaker steady GC showed it can intrude into the bay along the north shore without the anticyclonic eddy north of Miscou Island (a process of the attachment). Using a model domain without inclusion of the Gaspé peninsula coastal line shows that almost all the southward directed GC passed by the entrance of the BdC without intrusion. The findings above are related to the characteristics of the coastal current separation and are similar to the results of *Dengg* [1993] in a barotropic study of the Gulf Stream separation and analytical results from *Cherniawsky and LeBlond* [1986]. The separation problem is addressed by Gan et al. (submitted manuscript, 1995a; On the separation/intrusion of unsteady Gaspé current and variability in Baie des Chaleurs, I, Observations, submitted to *Journal of Geophysical Research*, hereinafter referred to as submitted manuscript, 1995b)

Comparing the observed circulation in the ML during September 1990 (Figure 2a) with corresponding model results in Figure 12, one finds that the predicted mean circulation agrees well with observations. Both of them show a cyclonic circulation pattern in the ML, with two gyres at the center and entrance of the bay. The fact that the mean observed current direction was eastward

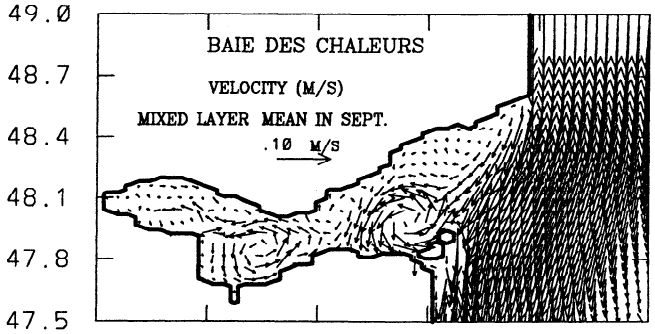

Figure 12. The mean circulation in the ML under observed atmospheric boundary forcing, Gaspé Current (GC), and river runoff in September 1990. The current speed is truncated at 0.1 m s^{-1}.

at O1 (Figure 2a) supports the hypothesis that the GC intrudes into BdC by the passage north of Miscou Island. Available observations in June 1990 also verify the existence of the anticyclonic eddy among stations O1, O2, and O3. In fact, this recirculation is controlled by the strength of GC separation as is discussed by Gan et al. (submitted manuscript, 1995a). Although no CTD data were available in 1990 and local meteorology data in 1991 are lacking (preventing us from directly comparing observed MLD), Figure 11 shows an ML trough at the entrance and a gradual shoaling toward the west of the bay, which is similar to the features in Figure 6. The similarity of model and observed MLD results suggests that the chosen GC strength was reasonable.

Similar to the horizontal distribution of h_1, the ML isotherms (Figure 11) tended to orient NW-SE, with a high slope in the center of the bay. This results from dynamical and thermodynamic interaction between the westward GC and prevailing westerly wind stress. In contrast to the case without GC (Figure 10), the upwelling along the north shore and in the western part of the bay was weakened by the GC intrusion. Therefore the colder and saltier water along the north coast comes mainly from advection from the GSL by the GC (details are in next section 4.4). As the outflow along the south shore transported warmer and less saline water toward the GSL, it formed a NW-SE tilt of the isotherms in the center of the bay. However, the stronger influence from separation/intrusion of the GC and the related eddies near the entrance of the bay resulted in concave isotherms. The spatial variability of the salinity and temperature fields results from the following two mechanisms: first, the resulting effects of local interaction between cold and salty water advected westward by the GC along the north shore and warm and brackish river runoff advected eastward by the westerly wind stress along the south shore; and second, the MLD variability which generated variability of thermal fluxes by entrainment and air-sea interaction (see discussion below). A strong thermal gradient occurred near the bay entrance (Figure 11), with warm and less saline water inside the bay. This fact may explain the use of 'chaleur' ("warm" in French) in the name of the bay.

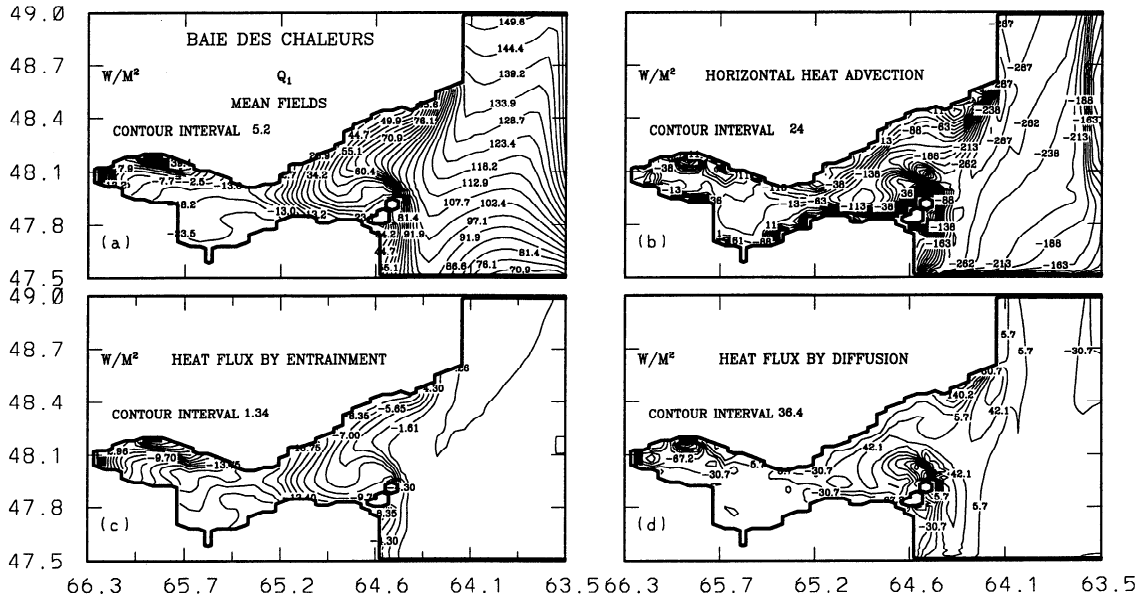

Figure 13. Horizontal distribution of 2-month mean of (a) surface heat flux Q_1, (b) horizontal heat advection, (c) heat fluxes by entrainment, and (d) by horizontal diffusion in the ML.

A qualitative comparison of the observed mean horizontal T_1 and S_1 distribution in summer 1991 (Figure 3) and model results (in 1990) in Figure 11 revealed that model results have a weaker NW-SE inclination of T_1 and S_1 contours at the central part of the bay. This, in fact, is due to a weaker GC separation (or its stronger intrusion near the north shore) in 1991, as is discussed by Gan et al. (submitted manuscript, 1995b).

Without direct wind forcing at the subsurface layer the intrusive GC generated a westward current (Figure 11). Similar to the ML, cyclonic gyres were formed in the central, western and eastern parts of the bay. This qualitatively agrees with the results in Figures 2a and 2b for subsurface circulation (about 30 m). The shallowest h_2 was located near the entrance of the bay, with the deepest one at the center. Compared with those in

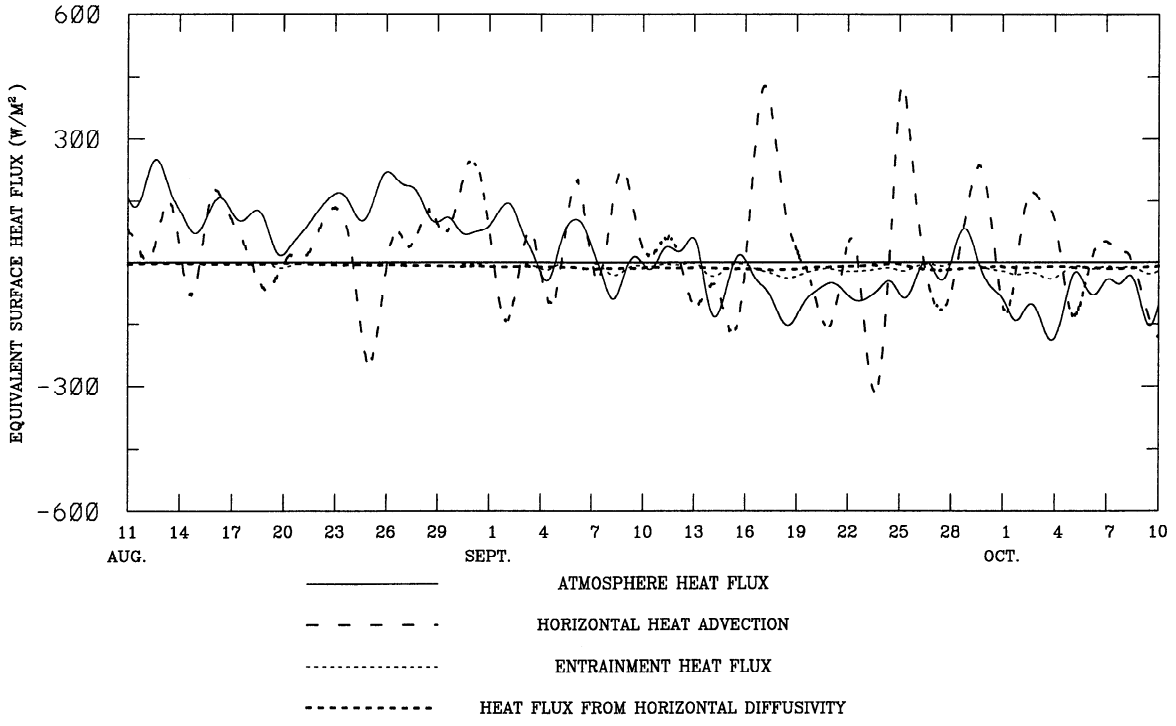

Figure 14. Time series of bay-averaged heat flux Q_1 and heat fluxes from horizontal advection, entrainment, and horizontal diffusivity in the ML.

the ML, horizontal variations of the temperature and salinity gradients were much weaker.

4.4. Thermal Balance in Baie des Chaleurs

In 3, the local sea surface temperature (SST) change is mainly controlled by the heat gain from the atmosphere Q_1, horizontal heat advection $Q_{ADV}=-h_1\mathbf{V}_1\nabla T_1\rho_0 C_p$, and vertical entrainment $Q_{WE}=W_e(T_e-T_1)\rho_0 C_p$. The flux Q_1 was the major heating/cooling source in the bay. The 2-month mean Q_1, which varied from about -20 W m^{-2} to 120 W m^{-2} (ocean gains heat with positive Q_1) from the interior to the entrance of the bay, is shown in Figure 13a. A distinct heat gain occurred at the entrance of the bay, where the cold GC intrusion generated a large thermal contrast between the surface and atmosphere over most of the integration period. The negative mean Q_1 inside the bay comes mainly from the strong heat loss to the atmosphere after mid-September, when air temperature dropped. The cold water advection (negative Q_{ADV}) by the GC was dominant near the entrance of the bay and gradually decreased toward the west (Figure 13b), resulting in warmer water in the interior of the bay (Figure 11). The mean positive Q_{WE} located at the entrance and in the GSL is due to detrainment induced by a strong positive atmospheric heat flux Q_1. In contrast, there is negative heat flux from entrainment in the western part of the bay (Figure 13c). The amount of mean heat flux from entrainment was much smaller than either Q_1 or the horizontal heat advection near the entrance. The horizontal heat advection and Q_1 therefore controlled the thermal balance at the east of the bay (east of station O6 in Figure 2), while the heat flux from entrainment was also important at the western part of the bay. The contribution from horizontal eddy diffusion, $Q_{DIFF}=K_m\nabla(h_1 T_1)\rho_0 C_p$, was large in areas with strong temperature gradients.

Each component of the heat flux was strongly time dependent and largely controlled by variability from either the dynamical forcing (e.g., GC and wind) or atmospheric fluxes. It should be emphasised that Figure 13 is the mean condition during warming (before September 7, $T_a>T_1$) and cooling seasons. Although mean Q_1 was positive at the GSL in both seasons, it was positive/negative in warming/cooling seasons inside the BdC, respectively. Since $Q_{WE}=0$. at the ML during the detrainment of the warming season, Q_{WE} can change ML temperature only in cooling season. Time series of bay-averaged (west of Miscou Island, hereinafter referred to as bay-averaged) heat fluxes for the ML (Figure 14) show that the fluctuations in Q_{ADV} correlated with those in westerly wind stress (Figure 5), while Q_1 was in phase with the air temperature. At the time of strong westerly winds a weaker GC intrusion generated a weaker westward cold advection.

As Q_1 became negative in cooling season, negative Q_{WE} occurred in the ML. Heat fluxes from entrainment and horizontal eddy diffusion were relatively small compared to Q_1 and Q_{ADV}. Along-shore heat advection was much stronger than the cross-shore component (not shown). The latter was mainly onshore warm advection due to westward current induced downwelling. In an experiment with the GC turned off, along-shore cold advection by intrusive GC was replaced by warm advection in eastward currents, although its magnitude

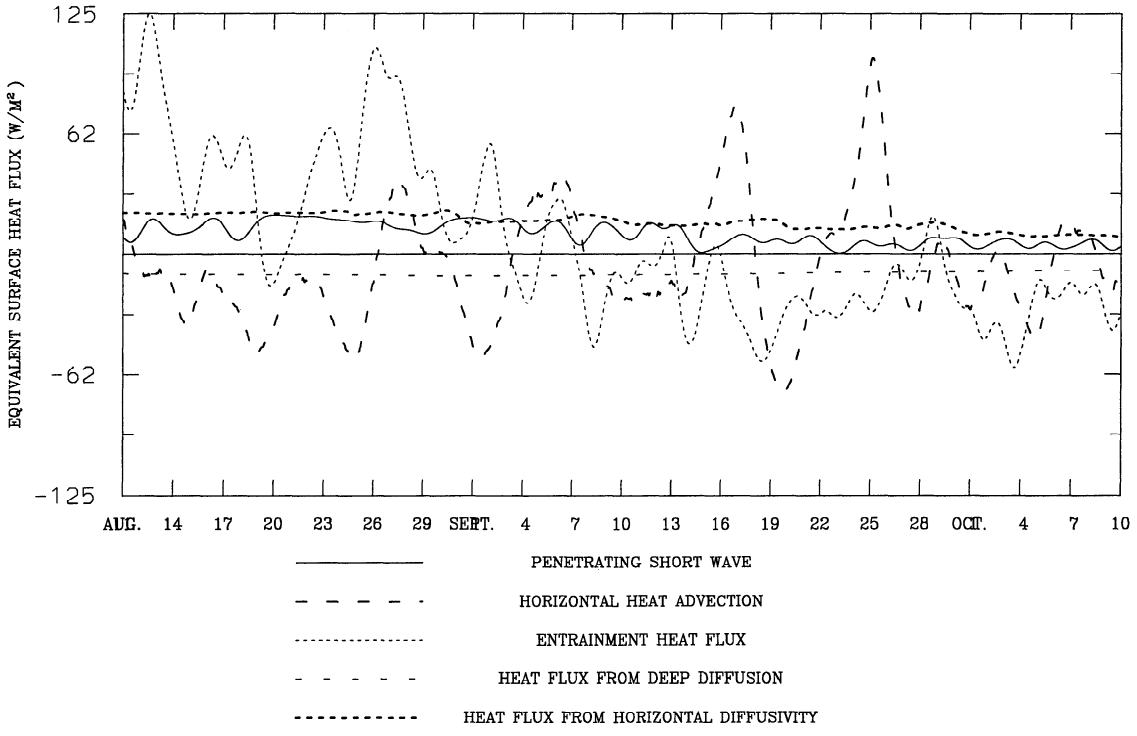

Figure 15. Time series of bay-averaged heat fluxes from penetrating shortwave, horizontal advection, entrainment, deep diffusion, and horizontal diffusivity at lower layer.

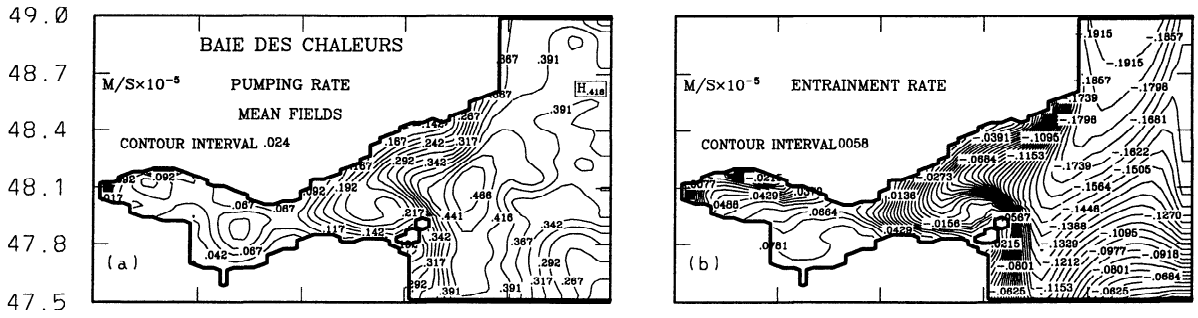

Figure 16. Two-month mean horizontal distribution of pumping rate and entrainment rate in the ML.

was much smaller. The corresponding offshore heat advection became negative and much larger when the GC was not included. As mentioned in sections 4.1 and 4.2, prevailing westerly winds resulted in upwelling along the north shore and decreased local SST by increasing entrainment. The corresponding larger cross-shore transport advected cold, upwelled water offshore. *Greatbatch* [1985] found that upwelling plays only a small role in changing SST, if the deepening due to entrainment is large compared with that due to upwelling. In BdC the horizontal divergence was several times larger than entrainment with or without GC (see section 4.5).

Time series of bay-averaged heat fluxes for the subsurface layer (Figure 15) showed that the heat flux was dominated by Q_{WE} and Q_{ADV}. During the detrainment in the ML (warming season), warmer water at the base of the ML was included into the second layer and increased T_2. However, when entrainment was generated in cooling season, the water at the interface with $T_e > T_2$ was removed from the top of the second layer. Therefore it caused a cooling of the lower layer when water was entrained into the upper layer. The heat fluxes from penetrating short wave and horizontal diffusion were relatively small as compared with Q_{WE} and Q_{ADV}, while the other components were all less than 10 W m^{-2} and were negligible.

4.5. Characteristics of the Mixed Layer Depth

The MLD is controlled by both divergence and entrainment (see (2)). The latter is governed by the balance between surface buoyancy fluxes and the effect of mixing due to wind- and buoyancy-generated turbulence.

The 2-month mean horizontal distribution of $W_o = -\nabla \cdot (h_1 \mathbf{V}_1)$, referred to as the pumping rate, and entrainment W_e, are shown in Figure 16. The mean pumping rate was much larger than entrainment in the eastern part of the bay, implying that horizontal divergence was the key factor in controlling the MLD there. In the western part of the bay, however, their magnitude was comparable. The westward current due to the GC intrusion downwelled the water and generated a positive mean value of W_o over the whole bay, with stronger values along the north shore and the entrance of the bay. Unlike the convergence field, entrainment was stronger on the south shore. In the GSL and north of the Miscou Island, water was mainly detrained. The main source for negative W_e in this area was the strong positive turbulent heat flux from the atmosphere (Figure 13) due to large air-sea temperature contrast resulting from cold GC advection. The combined effects from these two components controlled the mean ML depth distribution in Figure 11.

Time series of the bay-averaged pumping rate and entrainment (Figure 17) showed that a negative pumping rate (upwelling) in the cooling season decreased h_1 and increased entrainment. However, shallowing of the MLD due to upwelling in warm season would increase TKE from wind stress as well as turbulence heat flux in the ML at the same time. The opposite effects of TKE from wind stress and turbulence heat flux on the entrainment resulted in a weak response of W_e to upwelling. The mainly negative W_e in the warmer season and positive values in the colder season indicate the importance of turbulent heat flux on entrainment. As shown in Figure 5, wind stress increased and air

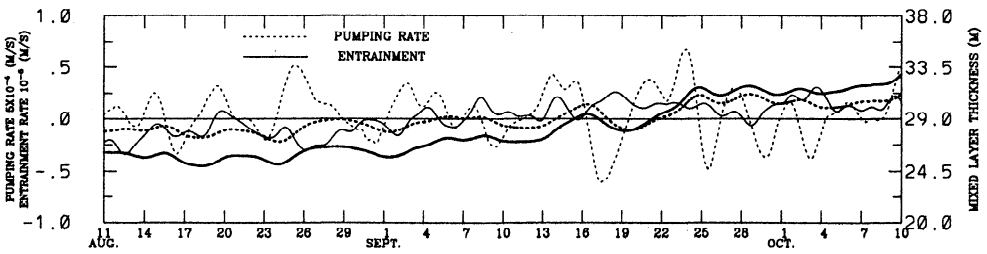

Figure 17. Times series of bay-averaged pumping rate and entrainment in the ML. The thick solid line refers to mean h_1 and the thick dashed line to mean h_1 when entrainment was not included.

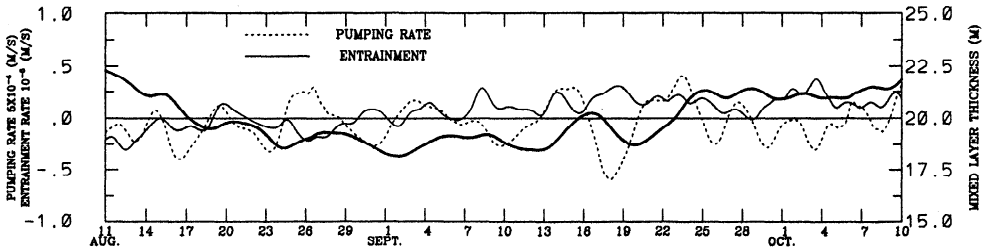

Figure 18. Times series of bay-averaged pumping rate and entrainment in the ML without GC. The thick solid line refers to mean h_1.

temperature dramatically decreased after September. Consequently, TKE from wind stress and negative Q_1 shifted the mainly negative W_e (detrainment) to positive (entrainment), which, in turn, deepened the ML. It is noteworthy that although W_e changed sign from warm to cooling seasons, its transient horizontal distributions had characteristics similar to the 2-month mean field. The rapid deepening of the mean ML as fall approached was mainly due to the higher entrainment, while the time-averaged increase in upwelling and downwelling effects nearly balanced each other. In contrast, the negative W_e in the warm season tended to shoal the ML, while the stronger GC deepened the ML. The typical entrainment (or detrainment) magnitude was 2-3×10^{-6} m s^{-1}, which can deepen (shoal) the ML by 3-8 m in 30 days. Therefore the timescale of entrainment effects on ML depth was more than a week.

To investigate the importance of entrainment, we carried out a test run in which the entrainment was set to zero. While the pumping rate was nearly unchanged, the bay-averaged h_1 deepened about 3-4 m during the warm season due to the loss of negative W_e and became shallower during the cold season due to the loss of positive W_e (Figure 17). The 2-month mean of T_2 decreased 1-1.5^{0}C and S_2 increased by about 0.3-0.6 parts per thousand (ppt) in the bay, while T_1 and S_1 had a weaker change (not shown). Without GC forcing, on the other hand, W_e/W_o were substantially increased/decreased (Figure 18). The dramatic decrease of the MLD shows the dominant effect of W_o on the MLD. It also suggests that the effects of the GC deepen the ML and suppress entrainment.

4.6. Variations in the Forcing

The variability of dynamics and thermodynamics in the bay was controlled by two major dynamical forcing mechanisms (wind stress and GC), as well as by buoyancy forcing (heat fluxes from atmosphere, river runoff). The effects of their variability are discussed in this section.

4.6.1. Variations in the wind. As mentioned above, the GC intrusion was a necessary condition for the generation of cyclonic circulation in the bay. However, when transient westerly wind stress dominated (Figure 19), eastward currents prevailed over the bay. The wind-induced upwelling led to ML shoaling in the western inner regions and a NE-SW orientation of h_1 contours near the entrance. The intrusive cold water west of Miscou Island shifted several kilometers eastward toward the GSL. At the time of strong easterly winds, intensified westward forcing enhanced the cyclonic circulation in the bay (Figure 20). It resulted in a stronger east-west gradient of h_1 and a NW-SE orientation of h_1 contours compared with the mean field (Figure 11). A correspondingly higher horizontal salinity and temperature gradient also occurred as cold water was pushed westward. The river plume was pushed back westward, and the cold water from the GSL advanced to the central part of the bay. Figures 19 and 20 also show the conditions for both the cold and warm season, which are reflected by their temperature and MLD fields (not shown).

4.6.2. Variation of the Gaspé Current. In the model the GC was assumed to be a steady feature. In reality, it varies with season and is possibly unstable [*Tang*, 1980; *Mertz and El-Sabh*, 1988]. Unfortunately, there are few observations available for the GC near our study area. Variability induced by different GC forcing is presented in this section.

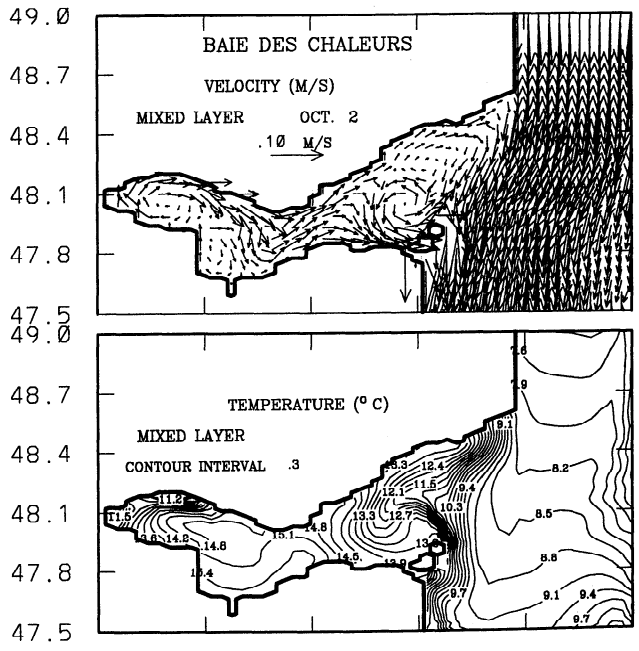

Figure 19. The circulation and temperature in the ML on October 2, 1990.

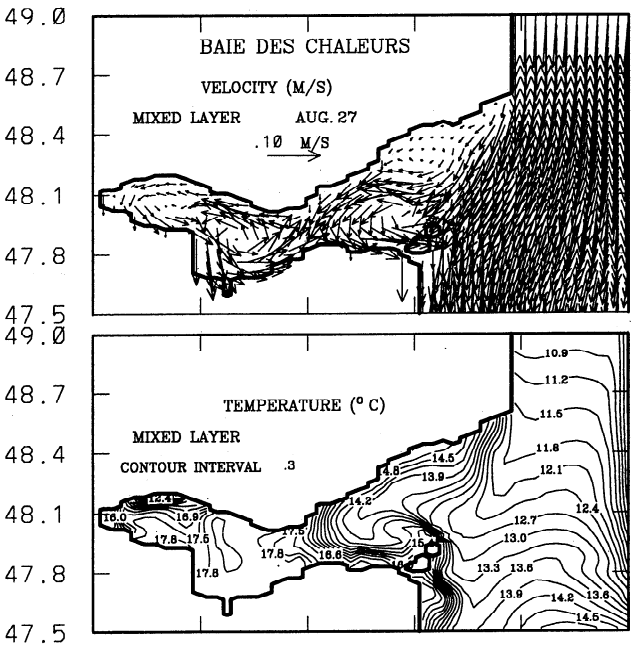

Figure 20. The circulation and temperature in the ML on August 27, 1990.

The importance of a varied GC can be seen from model-observation comparisons. A variable GC was constructed from (7), using the observed east-west, low-passed velocity component at station O6, the closest available station to the GC intrusion.

$$TRANSPORT_{GC} = -c_1[v_6(t) - v_0]\bar{h}W_i + c_2 \quad (7)$$

where v_6(t) is the east-west component of the measured current at station O6, and v_0 is an estimated wind-induced current. Here $\bar{h}$ is the mean MLD at the northern entrance of the domain, W_i is the width of the GC, and c_1 and c_2 are two constants controlling the strength of GC transport. The mean transport of the GC was set to be the same as the case for constant GC in the previous section, $1.3\text{x}10^5$ m^3 s^{-1} (Figure 21) . By comparing the constructed GC and the east-west component of wind stress, one finds that the GC increased about 3 days after increasing westerly winds in BdC. Since the wind stress in the northwest GSL has a phase close to that in the BdC (Gan et al., submitted manuscript, 1995b), the relation between GC and wind stress above agrees with the concept that the GC is mainly generated by the upwelling at northwest of the GSL [*Bugden*, 1981, *Mertz et al.*, 1988].

Figures 22a-22c show the time series of thickness, velocity, temperature, and salinity in the ML for both observation and model results for stations located near the north (O6, O9) and south (O7) shores (Figure 2a). Owing to coarse vertical resolution of the current meter moorings, a time series of h_1 could not be derived. However, time series of fluctuations of the interface between ML and the subsurface at stations O6 and O7 can be determined using available temperature data from current meter moorings, which were located in the upper

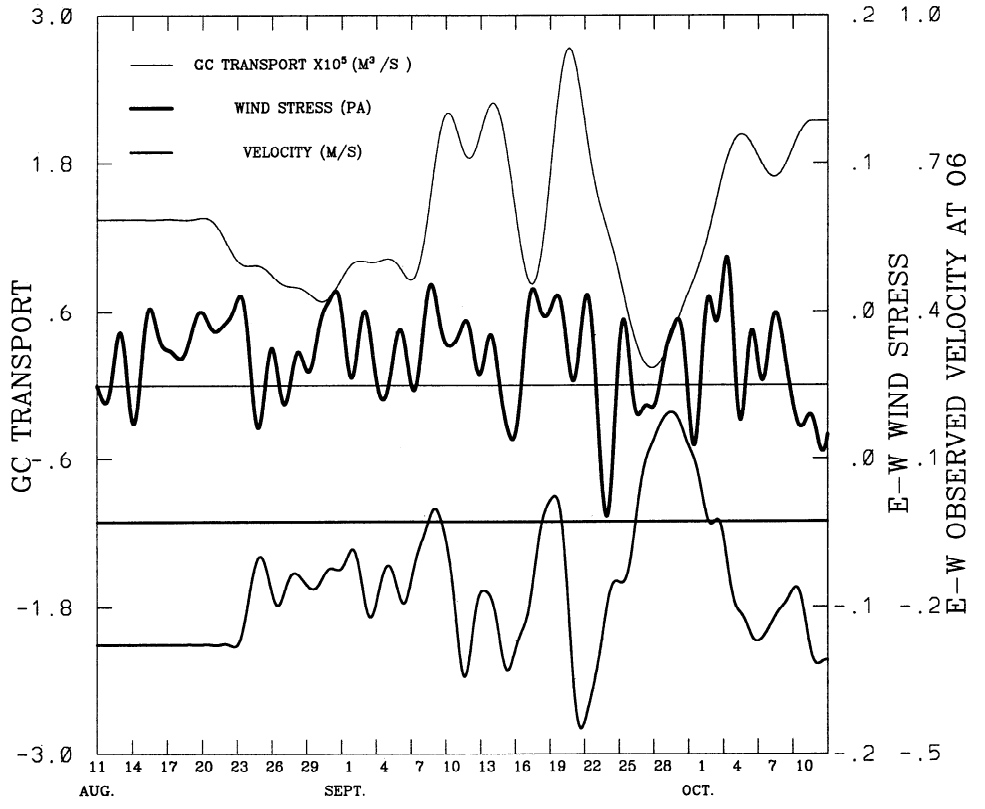

Figure 21. Time series of constructed GC transport, east-west velocity component at station O6, and east-west wind stress component.

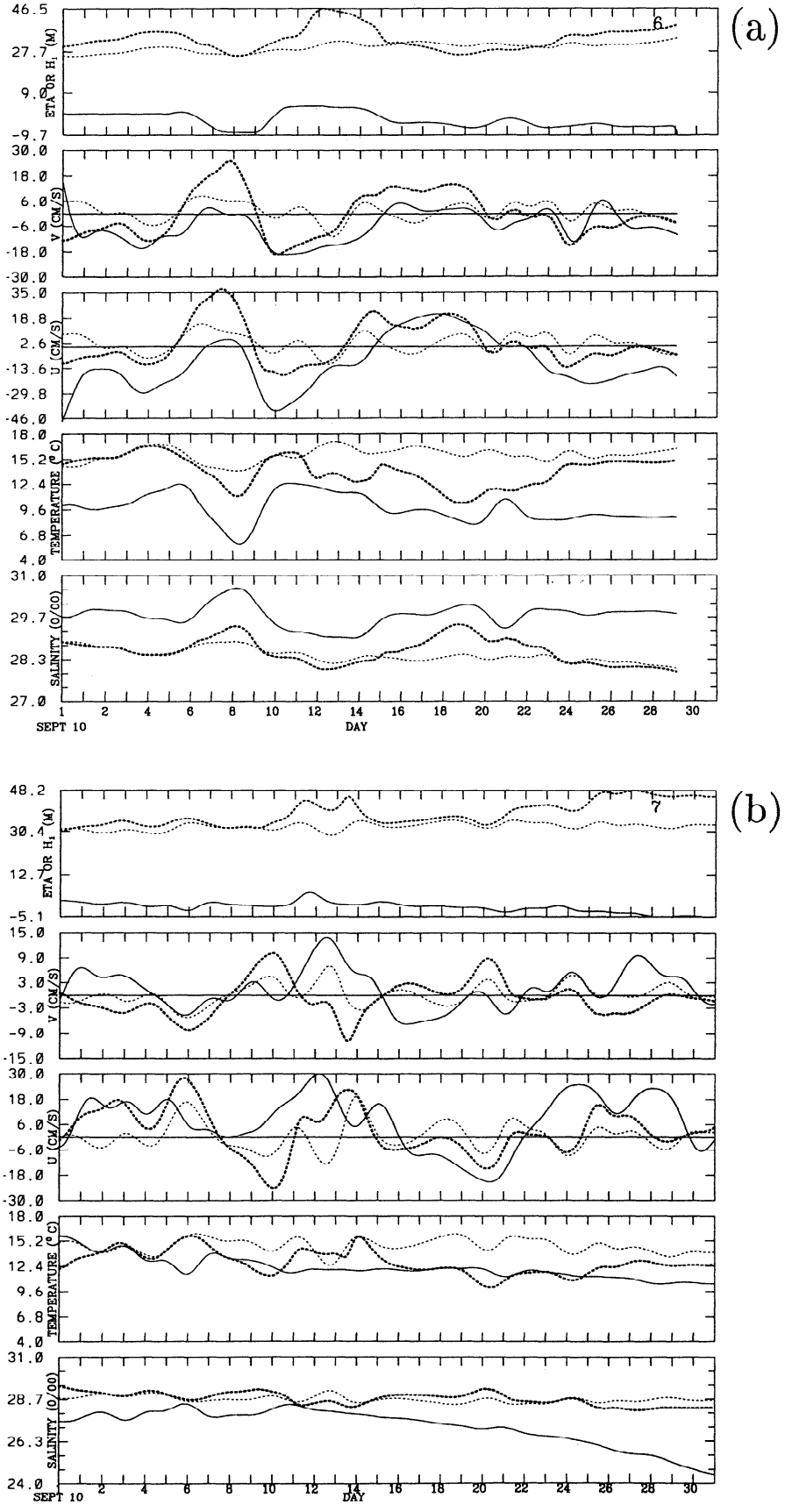

Figure 22. Time series of observed interface fluctuation (ETA) and predicted ML thickness H_1, velocity, temperature, and salinity for stations (a)O6, (b)O7, and (c)O9. Solid lines refer to observations. Thick and thin dashed lines are results from varied and constant GC, respectively.

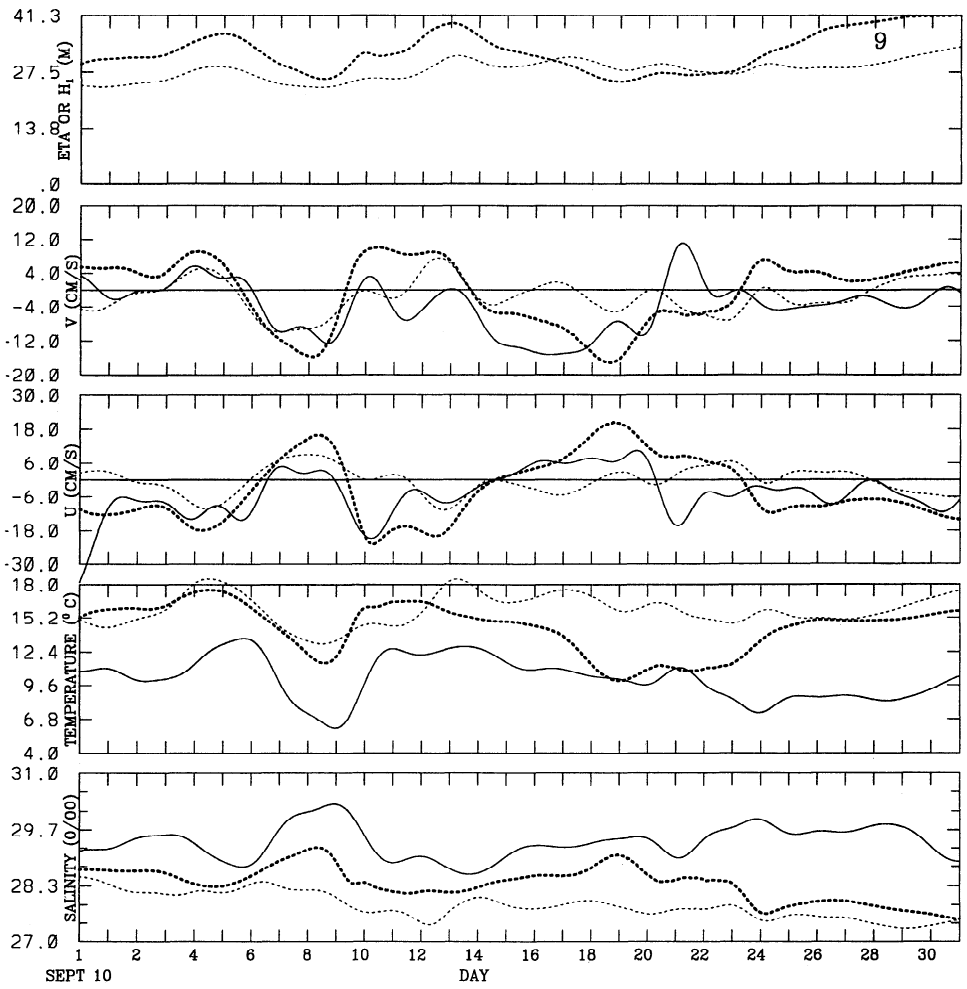

Figure 22. (continued)

and lower layers. The fluctuations are found by tracing an individual isotherm, as in Figure 4. To match the fixed depth observed data, T_1 and S_1 defined in the layer model were (approximately) corrected by a method similar to that used by *Price* [1981]:

$$[T(t), S(t)] = [T_1(t), S_1(t)] + [h_1(t) - H_0]\frac{\partial(T, S)}{\partial h} \quad (8)$$

where $\partial(T,S)/\partial h$ is the local temperature gradient between the base of the ML and middepth of pycnocline and H_0 is the mean ML thickness. The velocity comparisons were based on the assumption that vertical shear of horizontal velocity was small. Figures. 22a-22c show that the model underpredicted fluctuations of the ML, T_1 and S_1, especially the westward velocity when a constant GC transport was used. The results were substantially improved with a variable GC. In particular, the drop of GC transport (Figure 21) amplified the effects of westerly winds and hence upwelling at both stations O6 and O9 on September 18 (Figures 22a-22c).

Although the GC constructed here was only an approximation, it showed the importance of GC fluctuations. The 2-month means of the dynamical and thermodynamic fields were similar to the case with constant GC (Figure 11), although the mean cyclonic circulation was slightly intensified at the west inner part of the bay (not shown). Figure 23 compares weaker (1×10^5 m^3 s^{-1}), and stronger GC (1.6×10^5 m^3 s^{-1}) cases in the ML for September, as well as the case with a variable GC. A weaker GC enhanced the westerly wind effect on the ML, which suppressed downwelling along the north shore. The bay-averaged ML thickness decreased by about 4 m due to the stronger wind-induced upwelling in the interior of the bay (Figure 23c). The east-west pressure gradient induced by the GC decreased, leading to a weaker cyclonic circulation in the western inner part of the bay. The cold temperature front was pushed back eastward to the vicinity of Miscou Island. It increased the mean temperature in the bay by 0.5-1^{0}C. The opposite situations occurred when the stronger GC was applied. The intensified fluctuations in both dynamical and thermodynamic fields can also be seen in Figure 23 for the case of varying GC.

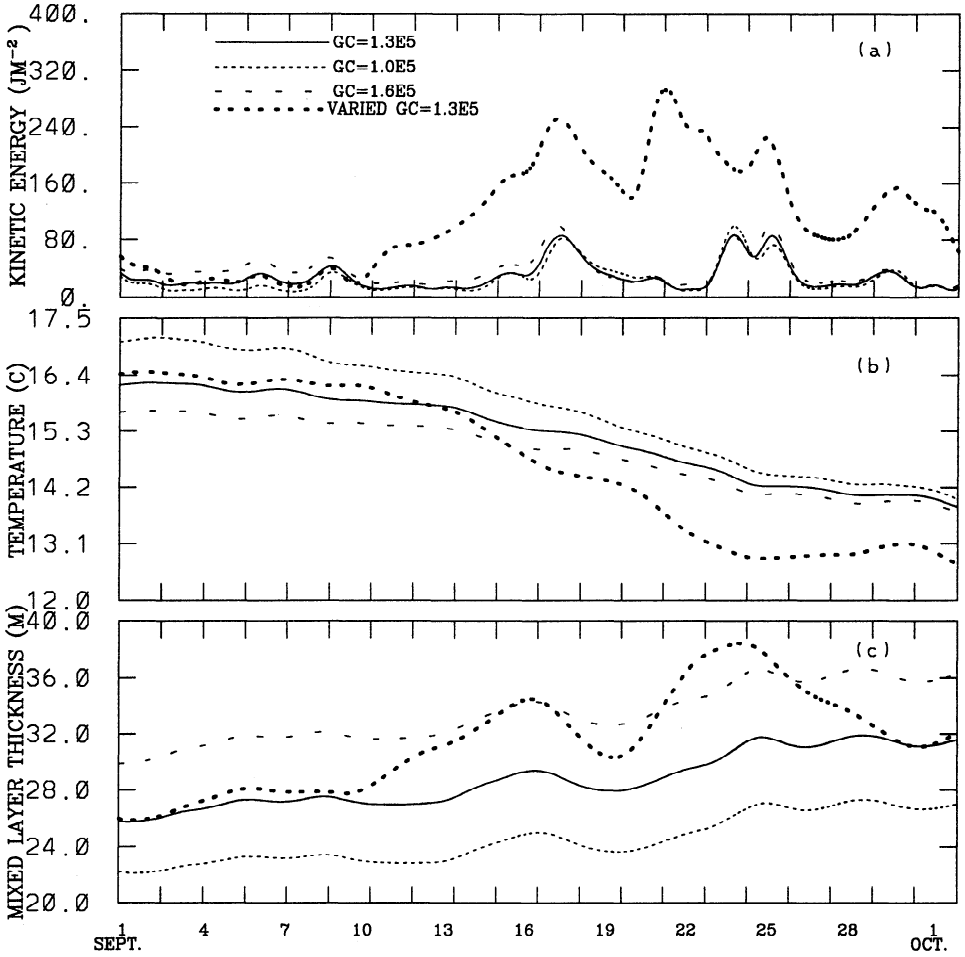

Figure 23. Time series of bay-averaged (a) kinetic energy (KE), (b) temperature, and (c) thickness at ML for four different GC strengths. Values are from averages over the inside of the bay (west of Miscou Island).

5. Summary and Conclusions

A 2 1/2 layer upper ocean model with an embedded bulk mixed layer model at the top was developed for a coastal region. The model consists of the ML and subsurface layer, which overlay a semipassive deep ocean. The entrainment and detrainment in the ML are determined by a Niiler-Kraus [*Niiler and Kraus,* 1977] type model. A high resolution (Δx=4 km, Δy=2 km) C-grid was adopted for the model. Proper numerical schemes and open boundary conditions were applied.

By forcing with observed atmospheric dynamics and thermodynamics, boundary inflow, and river runoff, the results showed that the model successfully simulated the circulation and thermal structure in the BdC. It is found that the cyclonic circulation in the bay was the dynamical response to intrusion of the Gaspé Current. The mean circulation was generally cyclonic, while an anticyclonic pattern occurred when strong, transient westerly winds dominated. Three cyclonic eddies were generated along the east-west axis of the bay. A weak anticyclonic eddy was also formed at the lee of the separated GC. Their strength depended on the forcing of wind and the intruding GC.

Cool and saltier water from the GSL was advected into the bay by the GC at its eastern entrance, which generated a strong thermal gradient between the GSL and the bay water and formed higher salinity and lower temperatures along the north shore. The water at the west of the bay was heated (or cooled in the cooling season) by atmospheric fluxes and diluted (salinity) by the river runoff. Heat flux from entrainment was also important in this part of the bay. The thermal balance in the ML at the east of the bay was mainly determined by larger-scale transport between the warmer bay and colder GSL and by atmospheric heating. In the subsurface layer the thermal balance was dominated by heat flux from both entrainment and horizontal advection.

Fluctuations in the ML thickness resulted from wind-related convergence and were intensified by GC variations. The timescale of entrainment or detrainment effects on the MLD was much longer than those resulting from the GC and wind-induced convergence. Without the GC forcing the convergence effect and hence the ML thickness was reduced, although entrainment was am-

plified. The varying GC intensified the wind-induced fluctuations in both the dynamic and thermodynamic fields. Given the strong dependence of the dynamics and thermodynamics in BdC on the GC, more accurate ML depths and fluctuations for the dynamic and thermodynamic fields can be only obtained when a more realistic description of the GC is available. We also realize the importance of the unsteady GC in determining the circulation characteristics in the bay. This topic is discussed by Gan et al., (submitted manuscripts, 1995a,b). The topography may affect the potential vorticity and hence the intrusion of the GC, although the strong stratification could decouple it from the GC which is mainly trapped near the surface.

Acknowledgments. We would like to thank P. Peltola, Claude Belanger, M.El-Sabh, J. C. Croteau, T. Vander Baaren, and C. le Quere for help in collecting and processing the data. Thanks also go to T. Warn for helpful discussions and Alan Schwartz for computing help. Field work was jointly supervised by El-Sabh, R.G.I. and other members of the OPEN Centre of Excellence. This work was supported by and is a contribution to the program of the Groupe Interuniversitaire de Recherche Oceanographiques du Quebec and OPEN (National Center of Excellence in Canada). Funds were also obtained from the Natural Science and Engineering Research Council of Canada (R.G.I. and R.J.G.) and the Fonds FCAR (R.G.I.).

References

Asselin, R., Frequency filters for time integrations, *Mon. Weather Rev., 100*, 487-490, 1972.

Benoit, J., and M. I. El-Sabh, Structure and seasonal characteristics of the Gaspe current, *J. Geophys. Res. 90*(C2), 3225-3236, 1985.

Budyko, M. I., *Climate and Life*, 66 pp, Academic, San Diego, Calif., 1974.

Bugden G. L., Salt and heat budgets for the Gulf of St. Lawrence, *Can. J. Fish. Aquat. Sci., 38*, 1153-1167, 1981.

Camerlengo, A. L., and J. J O'Brien, Open boundary conditions in rotating fluids, *J. Comput. Phys., 35*, 12-35, 1980.

Cherniawsky, J. Y., and P.H. LeBlond, Rotating flows along indented coastlines, *J. Fluid Mech., 169*, 379-407, 1986.

Cherniawsky, J. Y., C. W. Yuen, C. A. Lin, and L. A. Mysak, Numerical experiments with a wind- and buoyancy-driven two-and-a-half-layer upper ocean model, *J. Geophys. Res., 95*(C9), 16,149-16,167, 1990.

Dengg, J., The problem of Gulf Stream separation: A barotropic approach, *J. Phys. Oceanogr., 23*, 2183-2199, 1993.

Denman, K. L., A time-dependent model of the upper ocean, *J. Phys. Oceanogr., 13*, 173-184, 1973.

de Szoeke, R. A. and J. G. Richman, On wind-driven mixed layers with strong horizontal gradients A theory with application to coastal upwelling, *J. Phys. Oceanogr., 14*, 364-377, 1984.

El-Sabh, M.I., Surface circulation patterns in the Gulf of St.Lawrence, *J. Fish. Res. Board Can., 33*, 124-138, 1976.

Gan, J. P., R. G. Ingram, and R. J. Greatbatch, Sensitivity study of upper ocean model in a coastal bay. *J. Mar. Syst.* (in press), 1995.

Garwood, R. W., Jr., An oceanic mixed-layer model capable of simulating cyclic states, *J. Phys. Oceanogr., 7*, 455-471, 1977.

Greatbatch, R. J., On the role played by upwelling of water in lowering sea surface temperature during the passage of a storm, *J. Geophys. Res., 90*(C6), 11,751-11,755, 1985.

Greatbatch, R. J., and T. Otterson, On the formulation of open boundary conditions at the mouth of a bay, *J. Geophys. Res., 96*(C10), 18,431-18,445, 1991.

Gregory, D. N., O. C. Nadeau and D. Lefaivre, Current statistics of the Gulf of St. Lawrence and estuary, *Can. Tech. Rep. of Hydrogr. and Ocean Sci., 120*, 178pp, 1989.

Haltiner, G. J. and R. T. Williams. *Numerical Prediction and Dynamic Meteorology*, 2nd ed. 477 pp, John Wiley, New York, 1980.

Hsu, S. A., Correction of land-based wind data for offshore applications: A further evaluation. *J. Phys. Oceanogr., 16*, 390-394, 1986.

Kraus, E. B., and J. S. Turner, A one-dimension model of seasonal thermocline, II, The general theory and its consequences, *Tellus, 19*, 98-109, 1967.

Large, W. G. and S. Pond, Open ocean momentum flux measurements in moderate to strong winds. *J. Phys. Oceanogr., 11*, 324-336, 1980.

Lauzier, L. M., Bottom residual drift on the continental shelf area of the Canadian Atlantic coast, *J. Fish. Res. Board. Can., 24*, 1845-1959, 1967.

Legendre, L. and W. D. Watt, The distribution of primary production relative to a cyclonic gyre in Baie des Chaleurs, *Mar. Biol., 7*, 167-170, 1970.

LeQuere, C., Physical oceanography of the Baie des Chaleurs, Gulf of St. Lawrence. M.Sc. thesis, Dept. of Atmos. and Oceanic Sci., McGill Univ., Montreal, Que., 69pp, 1992.

McCreary, J. P., and P. Kundu, A numerical investigation of the Somali Current during the Southwest Monsoon, *J. Mar. Res., 46*, 25-58, 1988.

Mellor, G. L., and T. Yamada, A development of a turbulence closure model for geophysical fluid problems, *Rev. Geophys., 20*(4), 851-875, 1982.

Mertz, G., and M. I. El-Sabh, An autumn instability event in the Gaspé current, *J. Phys. Oceanogr., 19*, 148-156, 1988.

Mertz, G., M. I. El-Sabh, and P. Denis, Instability of a buoyancy-driven coastal jet: The Gaspe current and its St. Lawrence precursor, *J. Geophys. Res., 93*(C6), 6885-6893, 1988.

Mertz, G., V. G. Koutitonsky, and Y. Gratton, On seasonal cycle of Gaspé Current, in The Gulf of St. Lawrence: small ocean or big estuary?, edited by J.-C. Therriault, *Can. Spec. Publ. Fish. Aquat. Sci. 113*, 149-152, 1991.

Niiler, P. P., and E. B. Kraus, One-dimensional models of the upper ocean, in *Modelling and Prediction of the Upper Layers of the Ocean*, edited by E. B. Kraus, pp. 143-172, Pergamon, Tarrytown, N. Y., 1977.

Oberhuber, J. M., Simulation of the Atlantic circulation with a coupled sea ice-mixed layer- isopycnal general circulation model, I: Model description, *J. Phys. Oceanogr. 23*, 808- 830, 1993.

Paulson, C. A., and J. J. Simpson, Irradiance measurements in the upper ocean, *J. Phys. Oceanogr., 7*, 952-956, 1977.

Petrie, B., Monthly means of temperature, salinity and sigma-t for Gulf of St. Lawrence, *Can. Tech. Rep. of Hydrogr. and Ocean Sci., 126*, 137 pp, 1990.

Price, J. F., Upper ocean response to a hurricane, *J. Phys. Oceanogr., 11*, 153-175, 1981.

Schopf, P. S., and M. Cane, On the equatorial dynamics, mixed layer physics and sea surface temperature, *J. Phys. Oceanogr., 13*, 917-935, 1983.

Smagorinsky, J., General circulation experiments with the primitive equations, I, The basic experiment, *Mon. Wea. Rev., 91*, 99-164, 1963.

Tang, C. L., Mixing and circulation in the northwestern Gulf of St. Lawrence: A study of a buoyancy-driven current system, *J. Geophys. Res., 85*(C5), 2787-2797, 1980.

Tremblay, J. L., Rapport general sur les activites de la Station de biologie du St-Laurent pendant les annees 1936-1942, Rep. 4, pp 1-100, Univ. Laval, Ste-Foy, Que., 1943.

Trites, R. W., The Gulf of St. Lawrence from a pollution point of view, in *Marine Pollution and Sea Life*, edited by M. Ruivo, pp 59-72, FAO, Fishing News Books, London, 1972.

van der Baaren, A., C. Belanger, R.G. Ingram, and M. El-Sabh, Report of physical oceanographic data collected in the Baie des Chaleurs from 1990-1992 as part of the Ocean Production Enhancement Network (OPEN), data report, McGill Univ., Montreal, Quebec, 1992.

Yuen, C. W., J. Y. Cherniawsky, C. A. Lin, and L. A. Mysak, An upper ocean general circulation model for climate studies: Global simulation with seasonal cycle, *Clim. Dyn., 7*, 1-18, 1992.

Ping Chen, Program in Atmospheric and Oceanic Sciences, Princeton University, Princeton, New Jersey, P.O. Box CN 710, Sayre Hall, Princeton, NJ 08544-0710.

Jianping Gan and R. Grant Ingram, Department of Atmospheric and Oceanic Sciences, McGill University, Montreal, Canada, H3A 2K6.

Richard J. Greatbatch, Department of Physics, Memorial University of Newfoundland, St. John's, Newfoundland, Canada, A1B 3X7.

(Received June 3, 1994; revised March 24, 1994; accepted April 19, 1995.)